J. Fluid Mech. (1985), *vol.* 155, *pp.* 1–35
Printed in Great Britain

The onset of turbulence in finite-amplitude Kelvin–Helmholtz billows

By G. P. KLAASSEN AND W. R. PELTIER
Department of Physics, University of Toronto, Ontario, Canada M5S1A7

(Received 24 June 1983 and in revised form 5 July 1984)

Two-dimensional finite-amplitude Kelvin–Helmholtz waves are tested for stability against three-dimensional infinitesimal perturbations. Since the nonlinear waves are time-dependent, the stability analysis is based upon the assumption that they evolve on a timescale which is long compared with that of any instability which they might support. The stability problem is thereby reduced to standard eigenvalue form, and solutions that do not satisfy the timescale constraint are rejected. If the Reynolds number of the initial parallel flow is sufficiently high the two-dimensional wave is found to be unstable and the fastest-growing modes are three-dimensional disturbances that possess longitudinal symmetry. These modes are convective in nature and focused in the statically unstable regions that form during the overturning of the stratified fluid in the core of the nonlinear vortex. The nature of the instability in the high-Reynolds-number regime suggests that it is intimately related to the observed onset of turbulence in these waves. The transition Reynolds number above which the secondary instability exists depends strongly on the initial conditions from which the primary wave evolves.

1. Introduction

In Klaassen & Peltier (1985*a*, hereinafter referred to as KP), we described a sequence of numerical simulations of two-dimensional finite-amplitude Kelvin–Helmholtz (KH) waves. By using a higher level of resolution than was employed in previous numerical studies of these waves, we were able to trace the evolution of KH billows from initial states with Reynolds numbers as high as $Re = 900$, and were able to follow the flow histories from the regime of strong linear wave growth, through the subsequent nonlinear saturation of the wave amplitude, and into a regime in which the wave dynamics were dominated by diffusive decay. Although both observational and experimental evidence suggests that KH waves commonly break down into turbulence at some point in their evolution, no instabilities leading to the onset of chaotic motions were observed during the course of these two-dimensional numerical simulations. Since the simulations were continued to a point where the KH billows began to decay under the influence of diffusive processes, it seems certain that we have traced the evolution of these waves considerably beyond the time at which secondary instabilities should be initiated.

Whether or not the onset of turbulence will disrupt the evolution of a particular KH wave is in part determined by the values of the non-dimensional parameters associated with the initial parallel flow, namely the Reynolds number Re and the minimum Richardson number $Ri_{\min}$. The value of the Prandtl number Pr, which is a property of the fluid itself, will also play a role in determining the onset of chaos in these flows. If the critical Reynolds number governing the transition is low enough,

the onset of secondary instabilities may also depend on the characteristics of the disturbance that induces the growth of the primary KH wave. As pointed out in KP, this sensitivity to initial conditions is caused by the strong diffusion of the mean flow at low values of the Reynolds number.

Woods (1969) has made an explicit attempt to determine a value for the critical Reynolds number Re_c below which the onset of turbulence does not occur. He quotes a value of about 300 for a critical Reynolds number based on a lengthscale D given by the vertical amplitude of the billow and a velocity scale given by the 'overturning' speed. These are unfortunate choices because the amplitude of the KH wave is a function of the Reynolds number and the overturning speed is ill-defined. From the information we have, we may estimate $D \sim 4h$ and $V \sim \frac{3}{4}u_0$, where h is half the shear depth and u_0 is half the velocity difference across the shear layer. This gives a value of $Re_c \sim 100$ for the choice of scales we employ ($Re = u_0 h/\nu$). We should note that this observation is for $Pr \sim 10$ and that Woods (1969) failed to provide any information concerning the value of $Ri_{\min}$ for the KH waves he observed. Furthermore, this value of the critical Reynolds number lies in the region where the finite-amplitude characteristics of KH waves are extremely sensitive to the amplitude and structure of the disturbance that initiates wave growth (see KP).

Although neither Thorpe (1973) nor Koop & Browand (1979) have explicitly determined values for Re_c, their experiments have shown that the turbulent collapse of KH waves can occur for flows with $Re = 560$, $Ri_{\min} = 0.081$ and $Re = 75$, $Ri_{\min} = 0.075$ respectively. (Note that the values of all parameters have been converted to our choice of length- and velocity scales). In both cases the Richardson numbers are close to the value $Ri_{\min} = 0.07$ employed in our numerical simulations, while the Reynolds numbers are considerably lower than the maximum value $Re = 900$ that we have employed. However, these experiments pertain to a saline solution for which the Prandtl number $Pr \sim 700$, while our numerical simulations were performed with $Pr = 1$, a value representative of air. We therefore cannot entirely discount the possibility that finite-amplitude KH waves may be absolutely stable in the limited parameter range considered in KP.

However, there is another possibility, which presents a more attractive explanation for the failure of the numerical simulations described in KP to reveal the onset of turbulence. It is well known that fully developed turbulence involves chaotic motions in all three spatial dimensions. Furthermore, Thorpe (1973), Brown and Roshko (1974) and Koop & Browand (1979) have all reported that the onset of chaotic motions follows the introduction of fully three-dimensional motions into the shear layer. Since the numerical model we employed in our simulations of nonlinear KH waves (KP) was restricted to two spatial dimensions, it was not capable of representing any secondary instabilities leading to an intrinsically three-dimensional flow. This explanation for the failure of two-dimensional numerical models to reproduce the observed turbulent breakdown of KH waves, which was first proposed by Peltier, Hallé & Clark (1978), will be considered in more detail in what follows.

The experiments mentioned above have established that the collapse of KH billows involves a transition from a two-dimensional to a three-dimensional flow. In addition, Thorpe (1973) and Brown & Roshko (1974) have shown that the irregular small-scale motions associated with the onset of turbulence first appeared in the core of the KH wave. However, no attempt was made in these experiments to determine the physical origin of the secondary instabilities responsible for the turbulent breakdown of the nonlinear waves. Several mechanisms for this transition have been proposed in the literature. For example, Maslowe (1973) has suggested that small-scale secondary

Kelvin–Helmholtz disturbances may develop on the braids between adjacent vortex centres. Although such instabilities may occur, it is difficult to see how they could introduce three-dimensional motions into the shear layer. Furthermore, the observations clearly indicate that turbulence first appears in the core of the billow, forcing us to conclude that secondary instabilities of the braids are not likely to be involved in the onset of chaotic motions. Scorer (1969) proposed that a centrifugal instability could disrupt the circulating fluid in the core. Such an instability, which could introduce intrinsically three-dimensional motions into the core of the billow, would be consistent with the observations. Davis & Peltier (1979) have argued that the overturning fluid in the core could be disrupted by buoyancy forces, a process that would also produce secondary motions consistent with the observations.

In the present paper we test the two-dimensional nonlinear KH wave states of KP for stability against fully three-dimensional infinitesimal perturbations. This analysis is sufficient to determine which of these three mechanisms is responsible for the onset of turbulence in these flows. As in KP, we restrict our attention to Kelvin–Helmholtz waves with $Ri_{\min} = 0.07$ and $Pr = 1$. The effect of Prandtl number on the stability of nonlinear KH waves has been investigated in Klaassen & Peltier (1985*b*). The effect of the initial minimum Richardson number will be considered elsewhere.

We begin with a simple physical analysis concerning the possibility of gravitational instability (§2). The theoretical apparatus required to describe the evolution of general three-dimensional infinitesimal disturbances superimposed on the nonlinear two-dimensional KH wave is developed in §3. The rigorous calculation of the evolution of such disturbances is complicated by the fact that the nonlinear KH wave does not achieve a steady state at maximum amplitude, but rather begins a periodic exchange of energy with the mean flow. By restricting the analysis to those disturbances which grow quickly compared to the temporal variations in the background KH wave, we are able to reduce the problem to standard eigenvalue form. In §4 we outline the numerical technique used to solve these approximate equations. This is followed in §5 by an analysis of the stability of the KH wave with $Re = 500$. Since a preliminary search of wavenumber space has shown that the most unstable modes have their wave vector oriented parallel to the long axis of the KH wave, we restrict the presentation of our results to the case of longitudinal symmetry. Unstable modes with other wave-vector orientations will be discussed in future publications. In §6 we investigate the effect of the initial Reynolds number on the stability of KH waves and draw some conclusions concerning the critical Reynolds number for the onset of the instability. Our results are summarized in §7.

2. On the possibility of a buoyancy-induced instability

If simple parcel methods were applied to the stability analysis of nonlinear Kelvin–Helmholtz wave states, we should expect a gravitational instability to be realized in the regions of superadiabatic temperature gradient that form as the fluid in the core of the KH wave overturns. However, such crude arguments consider neither the diffusive properties of the fluid, nor the dynamics of the flow. Davis & Peltier (1979) pursued the question of a buoyancy-induced instability further by considering the superadiabatic regions that form in the core of the wave as thin, locally horizontal layers heated from below. In analogy with the Rayleigh–Bénard problem in the presence of a sheared mean flow (e.g. Kelly 1977), they proposed that unstable convective disturbances should take the form of rolls that are aligned in the direction of the shear. As Davis & Peltier pointed out, this preferred alignment for

unstable convective rolls would introduce an explicit dependence on the third spatial dimension into the Kelvin–Helmholtz flow.

Davis & Peltier tested this possibility by calculating a Rayleigh number representative of the superadiabatic regions at the time of maximum KH wave amplitude. It was found that this Rayleigh number increases dramatically between $Re = 400$ and $Re = 500$. The Rayleigh number corresponding to $Re = 450$ was found to be about 10^3, which is the same order of magnitude as the critical Rayleigh number for the Rayleigh–Bénard problem. Thus if the Reynolds number of the flow is sufficiently high, one would expect a buoyancy-driven three-dimensional instability to develop in the superadiabatic regions of the two-dimensional KH wave. However, since we are dealing with superadiabatic regions that are embedded in a sheared non-parallel flow, the analogy with the Bénard problem is not strictly valid. In order to establish rigorously the stability of a finite-amplitude Kelvin–Helmholtz wave one must perform a more sophisticated stability analysis.

Before proceeding to a more rigorous analysis, we shall find it instructive to examine the superadiabatic regions of the flow and their corresponding Rayleigh numbers in some detail. At time t we may define a local Rayleigh number associated with a fixed horizontal position x within a particular superadiabatic region by

$$Ra(x,t) = \frac{g\,\Delta\theta\,\delta^3}{T_0\,\kappa\nu}, \tag{2.1}$$

where $\Delta\theta(x,t)$ is the local change in potential temperature across the superadiabatic layer and $\delta(x,t)$ is the local depth of the layer (i.e. the vertical distance between points at which $\mathrm{d}\theta/\mathrm{d}z$ vanishes). This Rayleigh number may be expressed as a function of the primary non-dimensional parameters of the problem, namely the initial Reynolds number

$$Re = \frac{u_0 h}{\nu}, \tag{2.2}$$

the Prandtl number

$$Pr = \nu/\kappa \tag{2.3}$$

and the initial bulk Richardson number

$$Ri = \frac{gh\,\Delta T}{T_0\,u_0^2}, \tag{2.4}$$

such that

$$Ra = Re^2 Pr\,Ri \frac{\Delta\theta}{\Delta T}\left(\frac{\delta}{h}\right)^3. \tag{2.5}$$

Here h represents the half depth of the shear layer, while u_0 and ΔT respectively represent half the velocity and temperature differences across the layer. The cubic dependence on δ indicates that the Rayleigh number is very sensitive to the depth of the superadiabatic region. Also note that, in general, the factors $\Delta\theta$ and δ will be functions of Re, Pr and Ri as well as x and t.

Figure 1 illustrates the evolution of the potential-temperature field for the KH wave with $Re = 500$. The numerals labelling each plot refer to certain key times in the energy cycle of the wave, e.g. times at which the wave's Reynolds stress either vanishes or achieves an extreme value. Details are given in the caption, and further discussion may be found in KP. The shading in figure 1 indicates those regions in which the temperature gradient exceeds that for the adiabatic case. These superadiabatic regions are produced by overturning fingers of hot and cold fluid in the core of the KH billow. A small patch of statically unstable fluid first appears in the centre

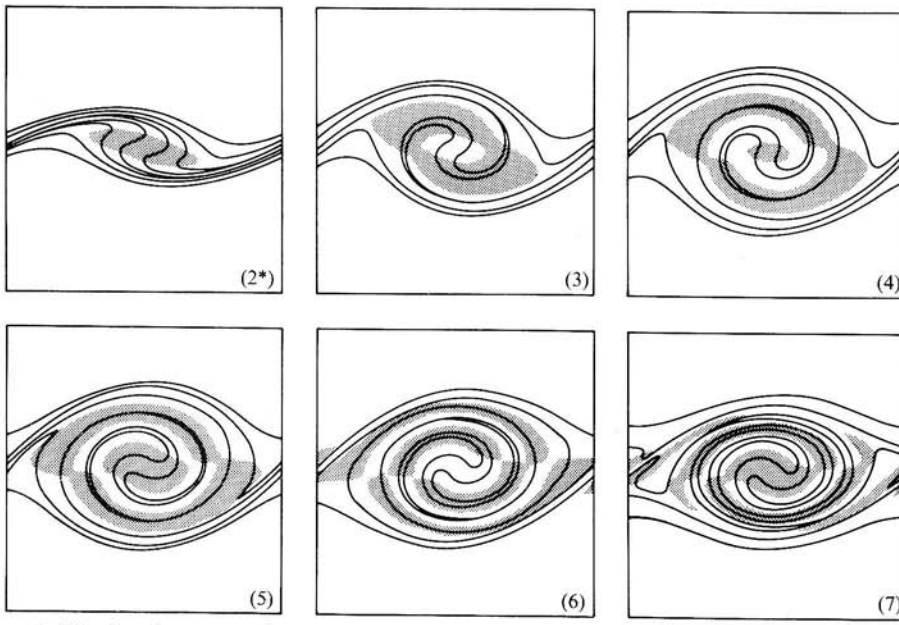

FIGURE 1. The development of statically unstable regions in the two-dimensional nonlinear KH wave with $Re = 500$. The regions where $d\theta^*/dz < 0$ (shaded areas) have been superimposed on sketches of the potential-temperature field at various key times in the wave's energy cycle, which are indicated in the lower-right corner of each frame: (3) maximum Reynolds stress, (4) maximum wave kinetic energy, (5) zero Reynolds stress, (6) minimum Reynolds stress, (7) zero Reynolds stress. Further details may be found in Klaassen & Peltier (1985*a*).

of the core at the key time (2*) ($t = 531.65$ s). This superadiabatic region (SAR) grows in size as the billow evolves, and after one complete revolution of the fingers it is transformed into a ring-shaped region (figure 1 (3)). This superadiabatic ring becomes narrower as it expands outward, and the next complete revolution of the fingers introduces another small patch of statically unstable fluid at the centre (figure 1 (4)). The process is repeated, and the core is gradually filled with successive rings of superadiabatic fluid. We shall find it convenient to refer to the first superadiabatic region to emerge as the primary SAR, the second as the secondary SAR, and so on.

It turns out that most of the spatial and temporal variations in Ra are due to variations in the depth δ, while the potential-temperature difference $\Delta\theta$ is relatively constant in both space and time. We have chosen the value of the Rayleigh number Ra^* at the centre of the domain ($x = \frac{1}{2}L$) and at the time of maximum wave amplitude (key time (4)) as a representative measure of the degree of stability. This choice provides the closest correspondence to the horizontal layer of the Bénard problem. Generally, both primary and secondary SARs exist at the key time (4). Since the value of Ra^* is considerably larger for the primary SAR, this region is the most likely site for the onset of secondary instabilities. We have calculated Ra^* for the primary SARs of various KH waves with initial Reynolds numbers in the range $300 \leqslant Re \leqslant 900$, and plotted it in figure 2 as a function of Re. If we assume that the critical Rayleigh number is of the order of 10^3, as it is in the Bénard problem, we would expect KH waves with initial Reynolds numbers greater than $Re \sim 300$ to be unstable to disturbances driven by buoyancy forces. However, in order to prove this conjecture, we must test the stability of these finite-amplitude waves against infinitesimal perturbations.

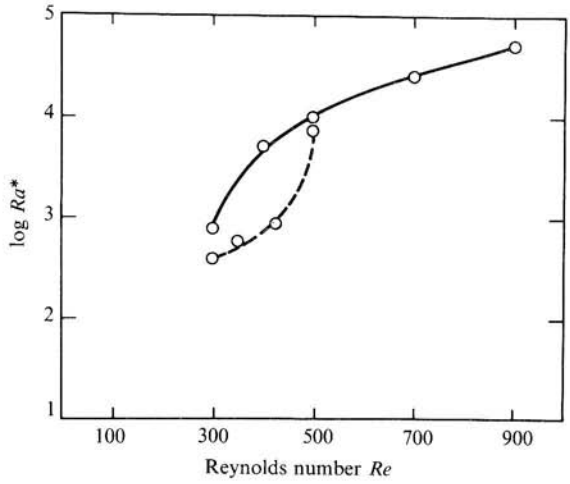

FIGURE 2. Common logarithm of $Ra^* = Ra(x = \frac{1}{2}L)$ at the time of maximum amplitude (key time (4)) for KH waves with various initial Reynolds numbers (solid line). The dashed line represents the result obtained by Davis & Peltier (1979), based on local averaging in the waves' superadiabatic regions.

3. A theory for the stability of Kelvin–Helmholtz waves

In this section we outline the method that we have developed for analysing the stability of two-dimensional finite-amplitude Kelvin–Helmholtz waves against fully three-dimensional infinitesimal perturbations. Although the numerical model employed in KP for the simulation of these waves was anelastic, we employ the Boussinesq equations for the stability analysis. This is permissible because the isentropic scale height $H_S = c_p \Theta/g$ of the fluid is large compared with the vertical extent $2h$ of the shear layer to which the KH flow is confined. Since the Boussinesq equations require the velocity field $\boldsymbol{u}_{\mathrm{B}}$ to be solenoidal (i.e. $\boldsymbol{\nabla}\cdot\boldsymbol{u}_{\mathrm{B}} = 0$), while the anelastic velocity field $\boldsymbol{u}_{\mathrm{A}}$ obeys the continuity relation $\boldsymbol{\nabla}\cdot[\bar{\rho}(z)\,\boldsymbol{u}_{\mathrm{A}}] = 0$, it is necessary to convert the anelastic velocity field to its Boussinesq counterpart by appropriate weighting with the anelastic background density profile $\bar{\rho}(z)$. We therefore employ the velocity field

$$\boldsymbol{u}_{\mathrm{B}} = \frac{\bar{\rho}(z)}{\rho_0}\,\boldsymbol{u}_{\mathrm{A}} \tag{3.1}$$

in the actual stability analysis. Here ρ_0 is the constant Boussinesq density.

In order to avoid the use of the pressure in the calculation of the temperature field, we have replaced the usual Boussinesq thermodynamic equation for the temperature deviation (e.g. Ogura & Phillips 1962) with an equation for the potential-temperature deviation. With this modification, the non-dimensional hydrodynamic equations in the Bossinesq approximation become

$$(\partial_t + u_j\,\partial_j)\,u_i = -\partial_i p^* + Ri\;\theta^*\delta_{i3} + \frac{1}{Re}\nabla^2 u_i \tag{3.2}$$

$$(\partial_t + u_j\,\partial_j)\,\theta^* = \frac{1}{Re\;Pr}\nabla^2\theta^*, \tag{3.3}$$

$$\partial_i u_i = 0, \tag{3.4}$$

where the potential temperature deviation

$$\theta^* = \frac{\theta - \Theta}{\Delta T} \tag{3.5}$$

has been non-dimensionalized with respect to ΔT (half the temperature difference) rather than Θ as in KP. We have chosen h (half the shear depth) and u_0 (half the velocity difference) as representative scales of length and velocity respectively. The non-dimensional parameters Re, Pr and Ri appearing in (3.2)–(3.4) have been defined previously in (2.2)–(2.4).

We linearize (3.2) and (3.3) by expanding the total Boussinesq velocity, potential-temperature deviation and pressure-deviation fields as

$$u_i(x,y,z,t) = \tilde{u}_i(x,z,t)\,(1-\delta_{i2}) + u_i'(x,y,z,t), \tag{3.6}$$

$$\theta^*(x,y,z,t) = \tilde{\theta}(x,z,t) + \theta'(x,y,z,t), \tag{3.7}$$

$$p^*(x,y,z,t) = \tilde{p}(x,z,t) + p'(x,y,z,t) \tag{3.8}$$

respectively. Here $\tilde{u}_i$, $\tilde{\theta}$ and $\tilde{p}$ represent the known two-dimensional finite-amplitude Kelvin–Helmholtz fields obtained from the numerical simulations described in KP, while u_i', θ' and p' represent the unknown three-dimensional infinitesimal perturbations. The coordinate system has been chosen to be compatible with that of KP, so that the x-axis ($i = 1$) is in the streamwise direction, the z-axis ($i = 3$) is in the vertical direction, and the y-axis ($i = 2$) defines the spanwise direction. Dropping all terms of second order in the perturbations and subtracting the equations for the two-dimensional KH flow, we obtain

$$\partial_t u_x' + \tilde{u}_x \partial_x u_x' + \tilde{u}_z \partial_z u_x' + (\partial_x \tilde{u}_x)\, u_x' + (\partial_z \tilde{u}_x)\, u_z' = -\partial_x p' + \frac{1}{Re}\nabla^2 u_x', \tag{3.9}$$

$$\partial_t u_y' + \tilde{u}_x \partial_x u_y' + \tilde{u}_z \partial_z u_y' = -\partial_y p' + \frac{1}{Re}\nabla^2 u_y', \tag{3.10}$$

$$\partial_t u_z' + \tilde{u}_x \partial_x u_z' + \tilde{u}_z \partial_z u_z' + (\partial_x \tilde{u}_z)\, u_x + (\partial_z \tilde{u}_z)\, u_z' = -\partial_z p' + Ri\,\theta' + \frac{1}{Re}\nabla^2 u_z', \tag{3.11}$$

$$\partial_t \theta' + \tilde{u}_x \partial_x \theta' + \tilde{u}_z \partial_z \theta' + (\partial_x \tilde{\theta})\, u_x' + (\partial_z \tilde{\theta})\, u_z' = \frac{1}{Re\,Pr}\nabla^2 \theta', \tag{3.12}$$

$$\partial_x u_x' + \partial_y u_y' + \partial_z u_z' = 0. \tag{3.13}$$

The relation (3.13) for the continuity of mass may be replaced by a diagnostic equation for the pressure:

$$\nabla^2 p' = Ri\,\partial_z \theta' - 2[(\partial_x \tilde{u}_x)\,\partial_x u_x' + (\partial_z \tilde{u}_z)\,\partial_z u_z' + (\partial_x \tilde{u}_z)\,\partial_z u_x' + (\partial_z \tilde{u}_x)\,\partial_x u_z'], \tag{3.14}$$

which is obtained by taking the divergence of the vector form of the momentum equations (3.9)–(3.11) and applying the solenoidal constraint (3.13). The boundary conditions at $z = 0$ and $z = H$ are

$$\left.\begin{aligned} &u_z' = 0, \quad \partial_z u_x' = \partial_z u_y' = 0, \\ &\theta' = 0, \quad \partial_z p' = \frac{1}{Re}\,\partial_z^2 u_z'. \end{aligned}\right\} \tag{3.15}$$

The boundary condition on the pressure perturbation is obtained from the vertical momentum equation (3.11) by applying the boundary conditions on θ' and u_i'.

The coefficients of the various terms in the linear homogeneous partial differential equations (3.9)–(3.14), which comprise the Kelvin–Helmholtz fields $\tilde{u}_x$, $\tilde{u}_z$ and $\tilde{\theta}$ and their derivatives, are independent of the y-coordinate and are periodic in x, with period $L = 2\pi/\alpha$. Since the solutions must remain bounded in the horizontal, they are of the form

$$f'(x, y, z, t) = \hat{f}(x, z, t)\, \mathrm{e}^{\mathrm{i}(bx+dy)}, \tag{3.16}$$

where f' is one of $\{u'_x, u'_y, u'_z, \theta', p'\}$, and b and d are real. Here $\hat{f}$ has the same period as the KH fields, i.e.

$$\hat{f}(x+L, z, t) = \hat{f}(x, z, t).$$

The x-dependence of (3.16) is dictated by an obvious parallel with the Floquet theory of ordinary differential equations (e.g. Jordan & Smith 1977). If the ratio b/α is rational then the solutions f' of (3.9)–(3.14) are periodic in the streamwise direction, with a period that is an integral multiple of L.

The substitution of (3.16) into (3.9)–(3.14) yields an initial-value problem, which may be rigorously solved by specifying the horizontal wavenumbers b and d and the initial disturbance fields $\hat{f}(x, z, t_0)$, and then integrating forward in time. However, this method has several disadvantages. Since the initial disturbances are arbitrary, it is not possible to ensure completeness, i.e. that all growing disturbances have been found. This problem may be reduced to a certain extent by initializing the $\hat{f}(x, z, t_0)$ with low-amplitude noise. However, one must then integrate the equations of motion for many time steps before the noise develops into a rapidly growing disturbance (see e.g. figure 14 of KP). If several competing modes existed and were simultaneously amplified, the results could be difficult to interpret. In the final analysis, this method would prove to be cumbersome and expensive.

Fortunately, there is an alternative approach available. Observations by Thorpe (1973) indicate that the disturbances involved in the secondary instability grow to finite amplitude very quickly when compared with the evolution of the original two-dimensional Kelvin–Helmholtz billow. On the basis of these observations, we assume that the flow evolves on two widely separated timescales, the slower timescale being associated with the background Kelvin–Helmholtz flow and the faster timescale being associated with the growth of the secondary instability. Then we may simply ignore the time dependence of the coefficients in (3.9)–(3.14). Since we are interested in disturbances that are unbounded in time, the perturbation fields would then have the form

$$f'(x, y, z, t) = f^{\dagger}(x, z)\, \mathrm{e}^{\mathrm{i}(bx+dy)+\sigma t}, \tag{3.17}$$

where $f^{\dagger}(x+L, z) = f^{\dagger}(x, z)$, and the growth rate is the real part of the complex variable σ. Substitution of (3.17) into (3.9)–(3.14) transforms this system into an eigenvalue problem.

The validity of the assumption concerning the separation of timescales can be subjected to *a posteriori* justification. Only those disturbances with growth rates much larger than the dominant frequencies of the power spectrum of the KH wave will be accepted as legitimate solutions of the eigenproblem. Note that it is therefore impossible to use this technique to locate neutral curves, a limitation which need not concern us here since we are only interested in those modes that will be physically realized, i.e. the fastest-growing modes. Although this method treats the Kelvin–Helmholtz wave as though it were in a steady state, we may gain some insight into the effect that the temporal variations of the KH background have on the secondary instability by applying the method at various instants in the evolution of the nonlinear wave.

Substituting perturbation fields of the form (3.17) into the linearized Boussinesq equations (3.9)–(3.14) yields the following set of stability equations:

$$\sigma u_x^\dagger + \tilde{u}_x(\partial_x + \mathrm{i}b)\, u_x^\dagger + \tilde{u}_z \partial_z u_x^\dagger + (\partial_x \tilde{u}_x)\, u_x^\dagger + (\partial_z \tilde{u}_x)\, u_z^\dagger = -(\partial_x + \mathrm{i}b)\, p^\dagger + \frac{1}{Re} \mathrm{L}_2 u_x^\dagger, \tag{3.18}$$

$$\sigma u_y^\dagger + \tilde{u}_x(\partial_x + \mathrm{i}b)\, u_y^\dagger + \tilde{u}_z \partial_z u_y^\dagger = -\mathrm{i}d p^\dagger + \frac{1}{Re} \mathrm{L}_2 u_y^\dagger, \tag{3.19}$$

$$\sigma u_z^\dagger + \tilde{u}_x(\partial_x + \mathrm{i}b)\, u_z^\dagger + \tilde{u}_z \partial_z u_z^\dagger + (\partial_x \tilde{u}_z)\, u_x^\dagger + (\partial_z \tilde{u}_z)\, u_z^\dagger = -\partial_z p^\dagger + Ri\, \theta^\dagger + \frac{1}{Re} \mathrm{L}_2 u_z^\dagger, \tag{3.20}$$

$$\sigma \theta^\dagger + \tilde{u}_x(\partial_x + \mathrm{i}b)\, \theta^\dagger + \tilde{u}_z \partial_z \theta^\dagger + (\partial_x \tilde{\theta})\, u_x^\dagger + (\partial_z \tilde{\theta})\, u_z^\dagger = \frac{1}{Re\, Pr} \mathrm{L}_2 \theta^\dagger, \tag{3.21}$$

$$(\partial_x + \mathrm{i}b)\, u_x^\dagger + \mathrm{i}d u_x^\dagger + \partial_z u_z^\dagger = 0, \tag{3.22}$$

$$\mathrm{L}_2 p^\dagger = Ri\, \partial_z \theta^\dagger - 2[(\partial_x \tilde{u}_x)\, (\partial_x + \mathrm{i}b)\, u_x^\dagger + (\partial_z \tilde{u}_x)\, \partial_z u_x^\dagger + (\partial_x \tilde{u}_z)\, \partial_z u_x^\dagger + (\partial_z \tilde{u}_z)\, (\partial_x + \mathrm{i}b)\, u_z^\dagger], \tag{3.23}$$

where the differential operator

$$\mathrm{L}_2 \equiv (\partial_x + \mathrm{i}b)^2 + \partial_z^2 - d^2. \tag{3.24}$$

We observe that (3.18), (3.20), (3.21) and (3.23) are closed with respect to the variables $u_x^\dagger$, $u_z^\dagger$, $\theta^\dagger$ and $p^\dagger$. When $d = 0$ the y-momentum equation decouples completely from the remainder of the eigensystem, and the eigenfunctions, which in this case are all independent of the y-coordinate, separate into two distinct classes. The first class comprise solutions of the subsystem defined by (3.18), (3.20), (3.21) and (3.23) (with $d = 0$), and have $u_y^\dagger = 0$. The second class comprise solutions of the subsystem consisting of the y-momentum equation (3.19) (with $d = 0$) and have $u_x^\dagger = u_z^\dagger = \theta^\dagger = p^\dagger = 0$. Since this latter class is not likely to be of any physical importance, it is ignored in the present study. When $d \neq 0$ the y-velocity eigenfunction $u_y^\dagger$ remains coupled to the rest of the eigensystem through the presence of the pressure term in (3.19). In this case $u_y^\dagger$ is superfluous in the sense that it need not be included in any scheme for the solution of the eigensystem.

The system of equations (3.18)–(3.23) possesses certain symmetries in the horizontal wavenumber space (b, d), which may be exploited to reduce the amount of computation required. The pertinent results may be summarized as follows.

I. If σ is an eigenvalue at (b, d) with eigenvector $(u_x^\dagger, u_y^\dagger, u_z^\dagger, \theta^\dagger, p^\dagger)$ then σ is also an eigenvalue at $(b, -d)$ with eigenvector $(u_x^\dagger, -u_y^\dagger, u_z^\dagger, \theta^\dagger, p^\dagger)$. (3.25)

II. If σ is an eigenvalue at (b, d) with eigenvector $(u_x^\dagger, u_y^\dagger, u_z^\dagger, \theta^\dagger, p^\dagger)$ then σ^* is an eigenvalue at $(-b, d)$ with eigenvector $(u_x^{\dagger *}, -u_y^{\dagger *}, u_z^{\dagger *}, \theta^{\dagger *}, p^{\dagger *})$. (3.26)

The first of these properties is a consequence of the fact that the eigensystem is invariant under the transformation $d \to -d$ and $u_y \to -u_y^\dagger$. The second may be established by putting $b \to -b$, $u_y \to -u_y^\dagger$ and taking the complex conjugate of each equation. These two results allow one to restrict the search for unstable modes to the quadrant where $b, d \geqslant 0$. In the case $b = 0$ the result (3.26) requires that the eigenvalues $\sigma = \sigma_R + \mathrm{i}\omega$ either be real or occur in complex-conjugate pairs. When

$\omega \neq 0$ the modes corresponding to σ and σ^* represent two waves travelling in opposite directions. Such modes, being simultaneously amplified, form stationary or standing waves.

We may gain some insight into the physical source of the unstable modes by constructing an equation for the y-averaged kinetic-energy density of these three-dimensional disturbances:

$$K''(x,z) = \tfrac{1}{2}(\overline{u_x'^2}^y + \overline{u_y'^2}^y + \overline{u_z'^2}^y), \tag{3.27}$$

where the averaging operator is defined by

$$\overline{(\ )}^y = \frac{1}{D}\int_0^D (\ )\,\mathrm{d}y, \quad D = \frac{2\pi}{d}. \tag{3.28}$$

It is straightforward but tedious to show that for $d \neq 0$ this equation is of the form

$$\begin{aligned} 2\sigma_{\mathrm{R}} K'' + (\tilde{u}_x \partial_x + \tilde{u}_z \partial_z) K'' \\ = -\tfrac{1}{2}(\partial_x \tilde{u}_x)\,|u_x^\dagger|^2 - \tfrac{1}{2}(\partial_z \tilde{u}_z)\,|u_z^\dagger|^2 - \tfrac{1}{2}(\partial_z \tilde{u}_x + \partial_x \tilde{u}_x)\,\mathrm{Re}\{u_x^{\dagger *} u_z^\dagger\} \\ + \tfrac{1}{2} Ri\,\mathrm{Re}\{u_z^{\dagger *} \theta^\dagger\} + \mathrm{PRESS} + \frac{1}{Re}\,\mathrm{DISS}, \end{aligned} \tag{3.29}$$

where PRESS contains all the terms involving the pressure perturbation $p^\dagger$ and DISS represents the dissipative terms. The terms on the right-hand side of (3.29) represent possible local sources and sinks of K''. The vertical heat flux correlations

$$\mathrm{HFLX} = \tfrac{1}{2}\, Ri\,\mathrm{Re}\{u_z^{\dagger *} \theta^\dagger\} \tag{3.30}$$

represent, if positive, the extraction of potential energy from the background KH flow, while the terms containing the velocity correlations

$$\mathrm{STR} = +\tfrac{1}{4}(\partial_x \tilde{u}_x - \partial_z \tilde{u}_z)\,(|u_z^\dagger|^2 - |u_x^\dagger|^2) - \tfrac{1}{2}(\partial_z \tilde{u}_x + \partial_x \tilde{u}_z)\,\mathrm{Re}\{u_x^{\dagger *} u_z^\dagger\} \tag{3.31}$$

are responsible for the exchange of kinetic energy with the background KH flow. Note the presence of the KH velocity-deformation fields in (3.31). The disturbance fields appear in the form of a Reynolds-stress correlation $-\mathrm{Re}\{u_x^{\dagger *} u_z^\dagger\}$, and also in the form $|u_z^\dagger|^2 - |u_x^\dagger|^2$. This latter quantity, if large and positive, indicates that there is little helicity (defined by $\boldsymbol{u}\cdot\boldsymbol{\nabla}\times\boldsymbol{u}$) present in the convection rolls. The sources of energy for the secondary instabilities may be determined by examining contour plots of the quantities in (3.30) and (3.31), as long as the y-wavenumber d does not vanish.

4. Numerical formulation of the stability problem

Several methods are available for the solution of the eigensystem (3.18)–(3.23). For example, one could take advantage of the periodicity in x to expand the disturbance fields in a Fourier series $f^\dagger(x,y) = \Sigma_\lambda\, g_\lambda(z)\, \mathrm{e}^{\mathrm{i}\lambda\alpha x}$, where $\alpha = 2\pi/L$. The resulting system of coupled ordinary differential equations in z could then be solved by a parallel shooting method (e.g. Keller 1976). However, the presence of the $(1/Re)\,(\mathrm{d}^2 g_\lambda/\mathrm{d}z^2)$ terms would necessitate the use of the notoriously inefficient algorithms required for the solution of stiff ODE systems, making this scheme much less attractive. Pierrehumbert & Widnall (1982) have used a version of the pseudospectral collocation method outlined by Boyd (1978) to solve a similar (though less complicated) problem concerning the stability of the steady nonlinear disturbances discovered by Stuart (1967) for an inviscid unstratified shear layer with a hyperbolic tangent velocity profile. We have elected to employ a Galerkin method similar to that used by Busse (1972) and Clever & Busse (1974) to test the stability of finite-amplitude

convection rolls. Each perturbation field is expanded in terms of a complete set of orthogonal basis functions, thereby converting the differential eigensystem (3.18)–(3.23) to an algebraic eigenvalue problem.

According to the boundary conditions (3.15), we may expand

$$u_x^\dagger = \sum_{\lambda=-\infty}^{\infty} \sum_{\nu=0}^{\infty} a_{\lambda\nu} F_{\lambda\nu}, \tag{4.1}$$

$$u_y^\dagger = \sum_{\lambda=-\infty}^{\infty} \sum_{\nu=0}^{\infty} r_{\lambda\nu} F_{\lambda\nu}, \tag{4.2}$$

$$u_z^\dagger = \sum_{\lambda=-\infty}^{\infty} \sum_{\nu=1}^{\infty} b_{\lambda\nu} G_{\lambda\nu}, \tag{4.3}$$

$$\theta^\dagger = \sum_{\lambda=-\infty}^{\infty} \sum_{\nu=1}^{\infty} c_{\lambda\nu} G_{\lambda\nu}, \tag{4.4}$$

$$p^\dagger = \sum_{\lambda=-\infty}^{\infty} \sum_{\nu=0}^{\infty} s_{\lambda\nu} F_{\lambda\nu}, \tag{4.5}$$

where

$$F_{\lambda\nu} = \mathrm{e}^{\mathrm{i}\lambda\alpha x} \cos\frac{\nu\pi z}{H}, \quad \partial_z F_{\lambda\nu}|_{z=0,\,H} = 0, \tag{4.6}$$

$$G_{\lambda\nu} = \mathrm{e}^{\mathrm{i}\lambda\alpha x} \sin\frac{\nu\pi z}{H}, \quad G_{\lambda\nu}|_{z=0,\,H} = 0. \tag{4.7}$$

If we make the substitutions (4.1)–(4.5) in the eigensystem (3.18)–(3.23), multiply each of the resulting equations by either $F^*_{\kappa\mu}$ or $G^*_{\kappa\mu}$ (whichever diagonalizes the term containing σ) and integrate over x and z using the operator defined in (3.26), we obtain the following algebraic system of equations:

$$\sigma a_{\kappa\mu} = \left(J^{(1)}_{\kappa\mu\lambda\nu} - \frac{A_{\lambda\nu}}{Re}\,\delta_{\kappa\lambda}\,\delta_{\mu\nu}\right) a_{\lambda\nu} + J^{(2)}_{\kappa\mu\lambda\nu}\, b_{\lambda\nu} - \mathrm{i}B_\kappa\, s_{\kappa\mu}, \tag{4.8}$$

$$\sigma r_{\kappa\mu} = \left(J^{(3)}_{\kappa\mu\lambda\nu} - \frac{A_{\lambda\nu}}{Re}\,\delta_{\kappa\lambda}\,\delta_{\mu\nu}\right) r_{\lambda\nu} - \mathrm{i}d s_{\kappa\mu}, \tag{4.9}$$

$$\sigma b_{\kappa\mu} = J^{(4)}_{\kappa\mu\lambda\nu}\, a_{\lambda\nu} + \left(J^{(5)}_{\kappa\mu\lambda\nu} - \frac{A_{\lambda\nu}}{Re}\,\delta_{\kappa\lambda}\,\delta_{\mu\nu}\right) b_{\lambda\nu} + Ri\, c_{\kappa\mu} + D_\mu\, s_{\kappa\mu}, \tag{4.10}$$

$$\sigma c_{\kappa\mu} = J^{(6)}_{\kappa\mu\lambda\nu}\, a_{\lambda\nu} + J^{(7)}_{\kappa\mu\lambda\nu}\, b_{\lambda\nu} + \left(J^{(8)}_{\kappa\mu\lambda\nu} - \frac{A_{\lambda\nu}}{Re\,Pr}\,\delta_{\kappa\lambda}\,\delta_{\mu\nu}\right) c_{\lambda\nu}, \tag{4.11}$$

$$\mathrm{i}B_\kappa\, a_{\kappa\mu} + \mathrm{i}d r_{\kappa\mu} + D_\mu\, b_{\kappa\mu} = 0, \tag{4.12}$$

$$A_{\kappa\mu}\, s_{\kappa\mu} = J^{(9)}_{\kappa\mu\lambda\nu}\, a_{\lambda\nu} + J^{(10)}_{\kappa\mu\lambda\nu}\, b_{\lambda\nu} - Ri\, D_\mu\, c_{\kappa\mu}, \tag{4.13}$$

where

$$B_\lambda = \lambda\alpha + b, \quad D_\nu = \frac{\nu\pi}{H}, \quad A_{\lambda\nu} = B_\lambda^2 + D_\nu^2 + d^2 \tag{4.14}$$

and summation is implied over repeated indices. The derivation of the interaction matrices $J^{(n)}_{\kappa\mu\lambda\nu}$, which consist of integrals typically of the form $\langle F^*_{\kappa\mu}\, \tilde{u}_z\, G_{\lambda\nu}\rangle$, is straightforward but tedious.

In order to eliminate the pressure terms from their stability equations, Clever & Busse (1974) formulated their analysis in terms of poloidal and toroidal velocity potentials. This procedure, which raises the order of the differential system, is unnecessary since (4.13) may be trivially solved for the Galerkin pressure coefficient $s_{\kappa\mu}$. Note, however, that this cannot be done in the special case $b = -\kappa\alpha$, $d = 0$,

$\mu = 0$, because then $A_{\kappa\mu} = 0$. Fortunately the indeterminate Galerkin pressure coefficient corresponding to this special case does not appear in (4.8)–(4.10), because $B_\kappa = d = D_\mu = 0$. Thus (4.13) may be used to eliminate $s_{\kappa\mu}$ from (4.8)–(4.10), giving

$$\sigma a_{\kappa\mu} = \left(I^{(1)}_{\kappa\mu\lambda\nu} - \frac{A_{\lambda\nu}}{Re}\,\delta_{\kappa\lambda}\,\delta_{\mu\nu}\right) a_{\lambda\nu} + I^{(2)}_{\kappa\mu\lambda\nu}\, b_{\lambda\nu} + Ri\left(\frac{\mathrm{i}B_\kappa D_\mu}{A_{\kappa\mu}}\right) c_{\kappa\mu}, \tag{4.15}$$

$$\sigma b_{\kappa\mu} = I^{(3)}_{\kappa\mu\lambda\nu}\, a_{\lambda\nu} + \left(I^{(4)}_{\kappa\mu\lambda\nu} - \frac{A_{\lambda\nu}}{Re}\,\delta_{\kappa\lambda}\,\delta_{\mu\nu}\right) b_{\lambda\nu} + Ri\left(\frac{\mathrm{i}D_\mu^2}{A_{\kappa\mu}}\right) c_{\kappa\mu}, \tag{4.16}$$

$$\sigma c_{\kappa\mu} = I^{(5)}_{\kappa\mu\lambda\nu}\, a_{\lambda\nu} + I^{(6)}_{\kappa\mu\lambda\nu}\, b_{\lambda\nu} + \left(I^{(7)}_{\kappa\mu\lambda\nu} - \frac{A_{\lambda\nu}}{Re\,Pr}\,\delta_{\kappa\lambda}\,\delta_{\mu\nu}\right) c_{\lambda\nu}. \tag{4.17}$$

Once (4.15)–(4.17) have been solved for $\{a_{\kappa\mu}, b_{\kappa\mu}, c_{\kappa\mu}\}$, (4.12) may be used to obtain the y-velocity eigenfunction $r_{\kappa\mu}$:

$$r_{\kappa\mu} = \begin{cases} -\dfrac{1}{d}[B_\kappa a_{\kappa\mu} - \mathrm{i}D_\mu b_{\kappa\mu}] & (d \neq 0), \\ 0 \quad (d = 0) & \text{(two-dimensional case).} \end{cases} \tag{4.18}$$

When $d \neq 0$ the value of $r_{\kappa\mu}$ so determined should satisfy

$$\sigma r_{\kappa\mu} = I^{(8)}_{\kappa\mu\lambda\nu}\, a_{\lambda\nu} + I^{(9)}_{\kappa\mu\lambda\nu}\, b_{\lambda\nu} + Ri\left(\frac{\mathrm{i}dD_\mu}{A_{\kappa\mu}}\right) c_{\kappa\mu} + \left(I^{(10)}_{\kappa\mu\lambda\nu} - \frac{A_{\lambda\nu}}{Re}\,\delta_{\kappa\lambda}\,\delta_{\mu\nu}\right) r_{\lambda\nu}. \tag{4.19}$$

When $d = 0$ the continuity equation (4.12) reduces to

$$\mathrm{i}B_\kappa a_{\kappa\mu} + D_\mu b_{\kappa\mu} = 0, \tag{4.20}$$

which may be used to independently verify the values of $a_{\kappa\mu}$ and $b_{\kappa\mu}$ obtained from (4.15)–(4.17).

In order to apply matrix-eigenvalue techniques we must cast (4.15)–(4.17) into the standard algebraic form

$$E_{ij}\, v_j = \sigma v_i \tag{4.21}$$

by truncating the expansions (4.1)–(4.4) at some finite wavenumbers $\lambda_{\max}$ and $\nu_{\max}$, and concatenating the Galerkin coefficients $a_{\lambda\nu}$, $b_{\lambda\nu}$ and $c_{\lambda\nu}$ into a single variable v with a single running subscript i. Details of an efficient method for the calculation of the matrix elements E_{ij} from the interaction matrices $I^{(n)}_{\kappa\mu\lambda\nu}$ are given in Klaassen (1982). The simplest truncation scheme one may apply to a two-dimensional Galerkin series is the so-called 'rectangular' truncation, where only those modes that satisfy $|\lambda| \leqslant N$, $0 \leqslant \nu \leqslant N$ are retained. However, such a scheme is wasteful of resolution, because it retains small coefficients in the vicinity of $\lambda \sim N$, $\nu \sim N$ while neglecting much larger coefficients near $\lambda \sim 0$, $\nu \sim N$ and $\lambda \sim N$, $\nu \sim 0$. Traditionally, this problem is avoided by adopting the 'triangular' scheme (Denny & Clever 1974; Clever & Busse 1974), which retains only those modes satisfying $|\lambda| + \nu \leqslant N$. However, this truncation scheme is not particularly well suited for use with the Galerkin basis (4.6)–(4.7). The function $\mathrm{e}^{\mathrm{i}\lambda_{\max}\alpha x}$ contains $2\lambda_{\max}$ half-wavelengths in the horizontal domain $L = 2\pi/d$, whereas $\sin(\nu_{\max}\pi z/H)$ contains only $\nu_{\max}$ half-wavelengths in the vertical domain H. Thus the truncation scheme $|\lambda| + \nu \leqslant N$ would not be optimal for a system where sufficient vertical resolution is crucial.‡ It has been found in practice that the modified triangular truncation scheme

$$2|\lambda| + \nu \leqslant N, \quad N = \text{odd integer}, \tag{4.22}$$

‡ If the instability is indeed confined to the vicinity of the superadiabatic regions, then the shape of that region (figure 1) suggests that vertical resolution should be more critical than horizontal resolution.

provides superior convergence in the present application. The scheme (4.22) reduces the matrix $\boldsymbol{E}$ to one or order

$$M = \tfrac{1}{2}(3N^2+2N+3). \tag{4.23}$$

Since the matrix is complex, it requires $2M^2$ real floating-point words of storage. Thus the storage requirements are roughly proportional to $4.5N^4$, so that even modest truncation levels place enormous demands on storage.

The algebraic eigensystem (4.21) was solved on the Cray 1a computer at the National Center for Atmospheric Research by using standard EISPACK subroutines (Smith *et al.* 1974). The largest matrix that could be stored in memory was that corresponding to the truncation level $N = 19$, for which $M = 562$. This truncation level was found to be the minimum acceptable for the determination of the eigenvalues in the present application. The demonstration of acceptable convergence at this maximum truncation level will be reported in what follows. The EISPACK routine CINVIT, which computes eigenvectors corresponding to selected eigenvalues by a method based on inverse iteration (see Smith *et al.* 1974), requires a work area equal in size to the original matrix. It therefore proved impossible to employ CINVIT for the recovery of eigenvectors beyond a truncation level of $N = 15$. A somewhat less general but more efficient routine based on a simple back-substitution technique was developed to retrieve eigenvectors for the truncation level $N = 19$. The details of this algorithm are given in Klaassen (1982).

Once the KH wave state whose stability is to be tested has been chosen and the horizontal wavenumbers b and d and the truncation level N have been specified, the matrix $\boldsymbol{E}$ may be computed and the eigensystem (4.21) solved. In order to ensure that the supposition (3.17) concerning the time dependence of the eigenfunctions is satisfied, we must discard modes with growth rates that are not large compared with the temporal variations in the two-dimensional KH flow. Since the KH wave is not steady, the growth rate obtained for a particular unstable mode will vary as the nonlinear KH wave evolves. Thus for a secondary instability to be realized, its growth rate must be maintained at an appreciable value for a length of time that is sufficient to permit the initial 'infinitesimal' disturbance to achieve a 'finite' amplitude. These criteria for the growth rates of physically realizable modes will be further refined in §5.

Although we may restrict our search for physical modes to those few with the largest growth rates, we cannot rely on the growth rate alone as a criterion to distinguish spurious from physically meaningful modes. The surface $\sigma(b, d)$ associated with a physical class of modes should converge as the truncation level N is increased, and should also display some degree of continuity with respect to the evolution of the Kelvin–Helmholtz background. Eigenfunctions corresponding to physical modes should not exhibit excessive structure on the scale of resolution, and should show signs of convergence as the resolution is increased. We note that this constitutes a particularly stringent test because eigenfunctions generally converge more slowly than the corresponding eigenvalues. In order to firmly establish the physical basis of a mode, it should be possible to correlate various features of the eigenfunction with the specific KH field from which it was derived.

5. Longitudinal modes of instability for the Kelvin–Helmholtz wave with $Re = 500$

We restrict ourselves in the remainder of this paper to examining the stability of nonlinear KH waves against infinitesimal disturbances with longitudinal symmetry, i.e. those disturbances with $b = 0$. This decision is supported by the fact that the

fastest-growing unstable modes were consistently found to have their horizontal wave vector, defined by $\boldsymbol{k} = b\tilde{\boldsymbol{x}} + d\hat{\boldsymbol{y}}$, oriented in the spanwise (y) direction. Also, Davis & Peltier (1979) have argued that the superadiabatic regions developing in two-dimensional finite-amplitude Kelvin–Helmholtz waves should become unstable against convection rolls. In analogy with the Rayleigh–Bénard problem in the presence of shear (e.g. Kelly 1977), these rolls would be aligned longitudinally, i.e. with their long axis in the direction of the shear vector. If the preferred mode of instability were centrifugal, it would also tend to have its wavevector oriented in the spanwise direction (e.g. consider the Taylor problem for the flow between rotating cylinders).

The Rayleigh numbers associated with the superadiabatic regions that develop in the KH wave with $Re = 500$, $Pr = 1$ and $Ri_{\min} = 0.07$ (see §2) indicate that these regions are quite likely to become gravitationally unstable. We therefore begin by examining in some detail the stability of this particular KH wave. The stability characteristics of KH flows with different initial Reynolds numbers will be dealt with in §6. It was shown in KP that the finite-amplitude KH wave oscillates about a state in which the net Reynolds stress vanishes and the major axis of the elliptical core of the billow is horizontal. Thus the KH wave state with vanishing net Reynolds stress, denoted by the key time (5) (see figure 2 and table 2 of KP), is the closest approximation we have to a stationary state. It would therefore seem appropriate to begin our examination of the stability of the nonlinear KH wave at this particular point in its evolution.

The growth rates and corresponding angular frequencies of various unstable modes of the $Re = 500$ KH wave at the key time (5) in its energy cycle have been plotted in figure 3 as a function of the spanwise wavenumber d. (The truncation level employed was the maximum, $N = 19$.) The various modes of instability displayed in figure 3 fall into several branches that are continuous in wavenumber space. Only those branches that have the largest growth rates and have been determined not to be spurious (according to the criteria outlined in §4) have been recorded in this figure. We recall from §3 that the structure of the stability equations forces the eigenvalues in this case ($b = 0$) to be either real or to occur in complex-conjugate pairs. The two modes corresponding to a complex-conjugate pair of eigenvalues are to be jointly interpreted as forming a stationary or standing wave that oscillates with a frequency given by $\omega/2\pi$.

Associated with each of the branches of unstable modes in figure 6(a) is an unique frequency that shows little variation with the wavenumber (figure 6b). We have grouped these branches into two distinct sequences; the reason for doing this will become apparent when we present the corresponding eigenfunctions. The first sequence has branches with frequencies $\omega_0 \approx 0$, $\omega_1 \approx \pm 0.17$, $\omega_2 \approx \pm 0.33$, $\omega_3 \approx \pm 0.54$ and $\omega_4 \approx \pm 0.70$ that occur in ratios of

$$|\omega_0| : |\omega_1| : |\omega_2| : |\omega_3| : |\omega_4| = 0 : 1 : 1.9 : 3.2 : 4.1,$$

while the second sequence has branches with frequencies $\omega_0' \approx 0$, $\omega_1' \approx \pm 0.26$ and $\omega_2' \approx \pm 0.49$ that occur in ratios of

$$|\omega_0'| : |\omega_1'| : |\omega_2'| = 0 : 1 : 1.9.$$

Thus the first sequence of branches (approximately) constitutes the first five harmonics of a Fourier spectrum with a fundamental frequency of $|\omega_1| \approx 0.17$. Presumably the growth rates of the branches corresponding to higher harmonics in this series are too small to be revealed by the present method. Only the first three

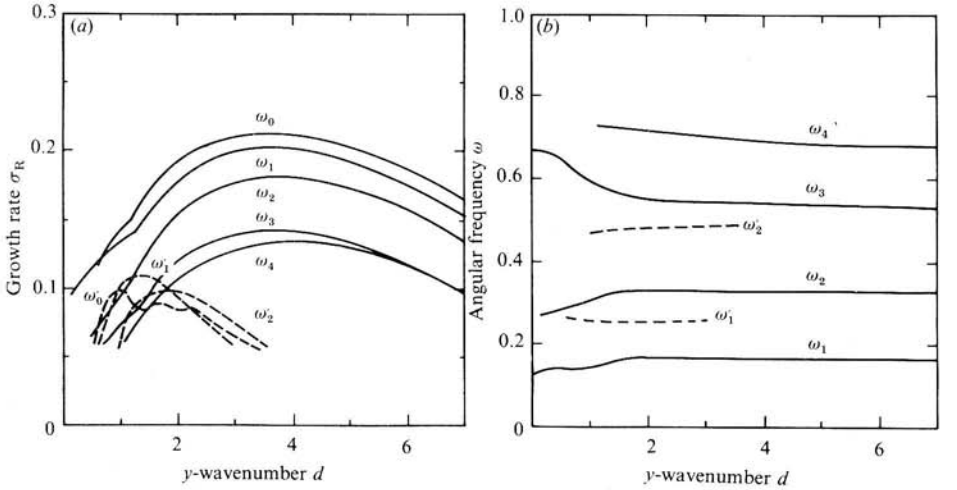

FIGURE 3. (*a*) The growth rate σ_R and (*b*) angular frequency ω as functions of the spanwise wavenumber d for various longitudinal ($b = 0$) unstable modes of the $Re = 500$ KH wave at the key time (5) in its energy cycle. The sequence of modes labelled $\omega_0, \ldots, \omega_4$ (solid lines) are associated with the primary SAR, while the $\omega_0', \ldots, \omega_2'$ modes (dashed lines) are associated with the secondary SAR. The truncation level used was the maximum $N = 19$.

Fourier harmonics are evident in the second sequence (that with fundamental frequency $|\omega_1'| \approx 0.26$), because the growth rates corresponding to these branches are substantially smaller than those of the first sequence.

In our presentations of contour maps of the eigenfunction correlations, we adhere to the convention of representing positive levels with solid lines and negative levels with dashed lines. Figure 4 contains plots of the perturbation vertical heat flux $\overline{u_z' \theta'}^y = \frac{1}{2} \operatorname{Re}\{u_z^{\dagger *} \theta^\dagger\}$ corresponding to the non-oscillatory and fundamental harmonics of the sequences with fundamental frequencies $|\omega_1| = 0.17$ and $|\omega_1'| = 0.26$. In order to compare eigenfunctions representative of the fastest-growing modes for each branch, we have fixed the wavenumber at $d = 3.6$ for the ω_1 sequence and $d = 1.15$ for the ω_1' sequence. In addition, the superadiabatic regions (SARs) of the $Re = 500$ Kelvin–Helmholtz flow at the key point (5) have been superimposed on each representation of the heat flux. Since a positive vertical heat flux is indicative of convective activity, it is apparent that the sequence of branches with fundamental frequency $|\omega_1| = 0.17$ correspond to convective activity in the primary (ring-shaped) SAR, while the sequence of branches with fundamental frequency $|\omega_1'| = 0.26$ correspond to convective activity in the secondary (oval-shaped) SAR at the centre of the billow's core. Similar correlations were found for the eigenfunctions corresponding to the higher harmonics $|\omega_2|$, $|\omega_3|$, $|\omega_4|$ and $|\omega_2'|$.

Plots of the correlations $\overline{u_x' u_z'}^y = \frac{1}{2} \operatorname{Re}\{u_x^{\dagger *} u_z^\dagger\}$ and $\overline{u_z'^2}^y - \overline{u_x'^2}^y = \frac{1}{2}\{|u_z^\dagger|^2 - |u_x^\dagger|^2\}$, which are responsible for the exchange of kinetic energy with the nonlinear KH wave (figure 5), show that they are also confined to the superadiabatic region. Inspection of (3.29) shows that the contributions of these correlations to the disturbance kinetic-energy density is multiplied by the deformation fields of the KH wave. Since the deformation fields are predominantly confined to the braids of the nonlinear wave, which lay outside the SAR, the kinetic-energy conversion terms make negligible contributions to the disturbance energy, and will not be considered further in this analysis. The nature of these correlations clearly indicates that the instability we have

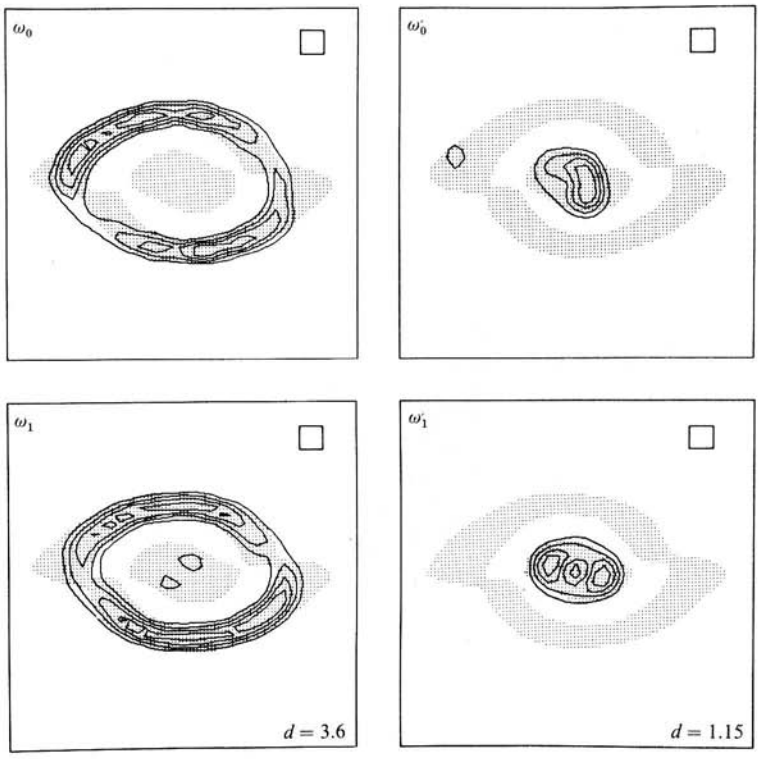

FIGURE 4. Vertical heat-flux correlations $\overline{\theta' u_z'}^y$ for several longitudinal ($b = 0$) unstable modes of the $Re = 500$ KH wave at the key time (5). The superadiabatic regions of the nonlinear wave (shaded area) have been superimposed on each frame. It can be seen that the ω_0 and ω_1 modes are associated with convective activity (positive heat flux) in the primary (ring-shaped) SAR, while the ω_0' and ω_1' modes are associated with convective activity in the secondary (oval-shaped) SAR. Note that the spanwise wavenumber d was chosen to be near that of the fastest-growing mode for each branch (i.e. $d = 3.6$ for the ω_0 and ω_1 branches and $d = 1.15$ for the ω_0' and ω_1' branches). The box in the upper right corner, which has dimensions of $L/(N-1)$ by H/N, shows the nodal spacing of the highest-order Galerkin functions $\exp(\mathrm{i}\lambda_{\max}\alpha x)$ and $\sin(\nu_{\max}\pi z/H)$.

discovered is not centrifugal in origin. Furthermore, it bears no resemblance to the translative instability discovered by Pierrehumbert & Widnall (1981) for the Stuart vortex in an unstratified free shear layer.

It is interesting to compare the growth rate of the most-unstable convective mode (i.e. the ω_0 mode with $d \approx 3.6$), given by $\sigma_{\mathrm{R}} = 0.213$, with the growth rate σ_{p} predicted by the simple parcel method of stability analysis. This method may be used to obtain a rough estimate of the rate at which a fluid parcel would be displaced from its initial level in an unstably stratified (but hydrostatic) environment, and gives

$$\sigma_{\mathrm{p}} = \frac{h}{u_0}\left[\frac{g}{\bar{\theta}}\left|\frac{\mathrm{d}\bar{\theta}}{\mathrm{d}z}\right|\right]^{\frac{1}{2}}. \tag{5.1}$$

Here we have multiplied by h/u_0 to obtain a non-dimensional value. We may estimate $\bar{\theta} \sim \Theta$ and $\mathrm{d}\bar{\theta}/\mathrm{d}z \sim \Delta\theta^*/\delta^*$, where $\Delta\theta^*$ is the potential-temperature contrast across the centre of the superadiabatic layer of the KH wave and δ^* is the depth of this layer. Since $\Delta\theta^* \sim 1.3\Delta T$ and $\delta^* \sim 0.66h$ for the primary SAR of the KH wave at

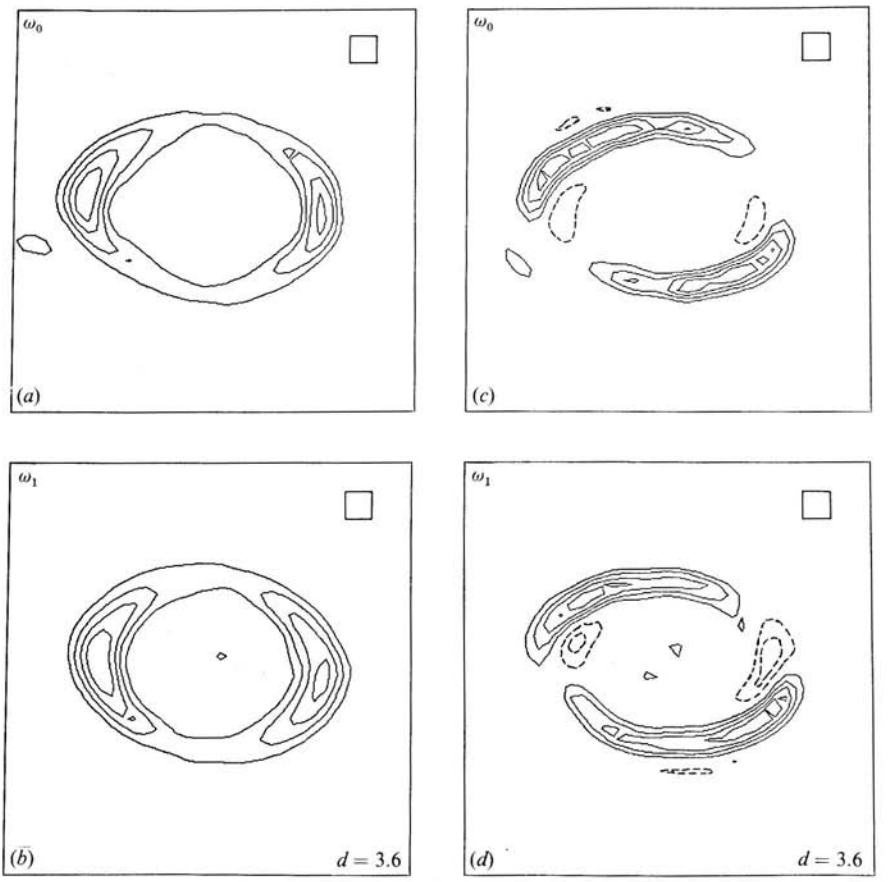

FIGURE 5. (*a*), (*b*) Reynolds stress ($-\overline{u_x' u_z'}^y$) and (*c*), (*d*) $\overline{(u_z')^2}^y - \overline{(u_x')^2}^y$ correlations for the ω_0 and ω_1 modes displayed in figure 4. Note that these correlations are confined to the superadiabatic region.

the key time (5), we obtain a growth rate $\sigma_p \approx 0.35$. The close correspondence between this crude estimate σ_p and the actual growth rate σ_R of the most-unstable mode revealed by our more rigorous stability analysis provides further support for our contention that the unstable modes we have discovered derive the major part of their energy from the unstable density stratification.

All results of the stability analysis presented to this point have been calculated with the maximum obtainable value of the truncation level $N = 19$. In order to obtain some idea of the accuracy of the eigenvalues and eigenfunctions at this level of truncation, we now turn our attention to the question of convergence. Figure 6 illustrates the dependence of the growth rates corresponding to $\omega_0' = 0$, $\omega_0 = 0$, $\omega_1 = \pm 0.17$ and $\omega_2 = \pm 0.35$ on the truncation level N. As a matter of interest, nearly 60 % more coefficients are retained in the Galerkin expansion at $N = 19$ than that at $N = 15$, while nearly 80 % more coefficients are retained at $N = 15$ than at $N = 11$. Note that, in the sequence of branches with fundamental frequency $|\omega_1| = 0.17$, there is a general trend for the wavenumber of the fastest-growing mode of a particular branch to increase as the truncation level increases. Convergence at long wavelengths is acceptable for all modes. While convergence near the wavenumber of maximum

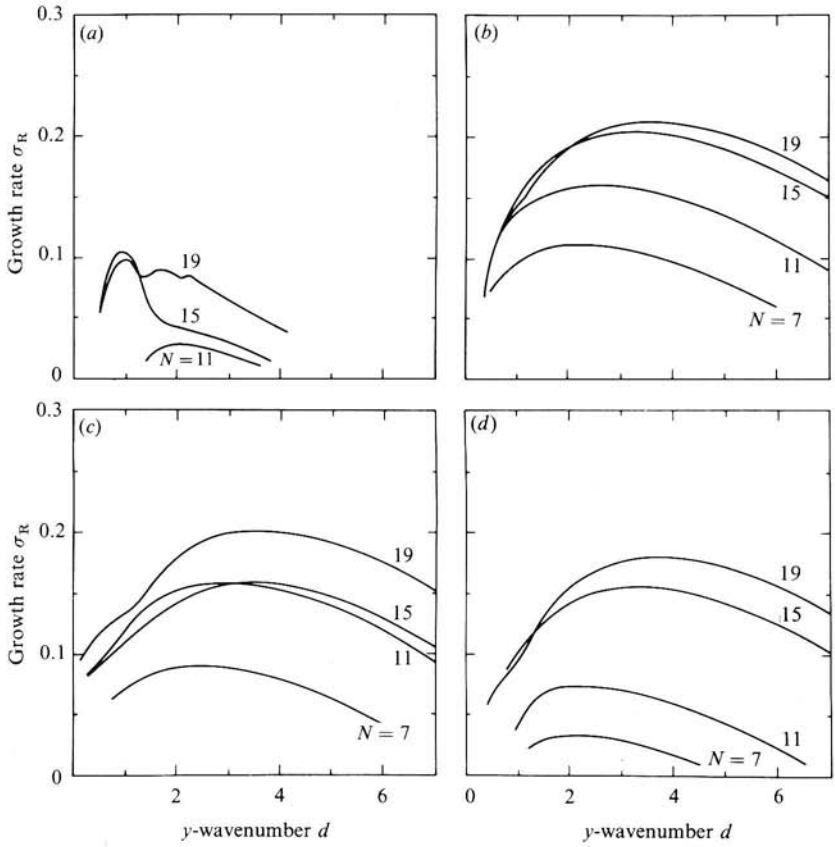

FIGURE 6. Convergence of the growth rates σ_R for the unstable longitudinal modes (*a*) ω_0', (*b*) ω_0, (*c*) ω_1 and (*d*) ω_2 of the $Re = 500$ KH wave at the key time (5). The numbers labelling each curve refer to the truncation level N, where $2|\lambda| + \nu < N$.

growth is excellent for the non-oscillatory modes, it is not quite as good for the oscillatory modes. We have not attempted to demonstrate the convergence of the branches corresponding to the frequencies ω_3, ω_4, ω_1 and ω_2' because the growth rates of these modes are generally too small to permit their accurate identification below truncation levels of about $N = 15$. Instead, as an indication of which modes are identifiable at the various truncation levels, we have recorded in table 1 the value of the frequency corresponding to each of the oscillatory branches as a function of the truncation level N.

Since small errors in an eigenvalue can often lead to large errors in the corresponding eigenfunction, eigenvalues generally converge more quickly than eigenvectors. Thus an examination of the variation of the eigenfunctions with the truncation level is a very stringent test of convergence. Figure 7 illustrates the convergence of the eigenfunctions corresponding to the frequencies ω_0 and $|\omega_1|$ at $d = 3.6$, which is close to the wavenumber of the fastest-growing mode. The vertical heat-flux correlations for $N = 11$ and $N = 15$ in figure 7 are to be compared with the corresponding representations of the eigenfunctions at $N = 19$ displayed previously in figure 4. The ω_1 mode shown in figure 6(*c*) shows little change when the truncation level is increased from $N = 11$ to $N = 15$ and a much larger change from $N = 15$ to $N = 19$. Since the

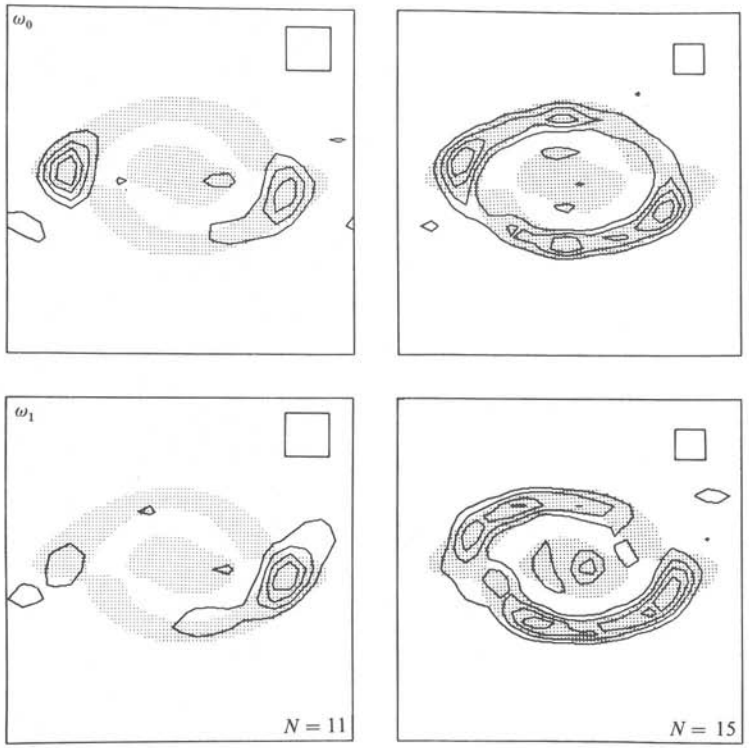

FIGURE 7. Convergence of the vertical heat-flux correlations ($\overline{\theta' u_z'^{\nu}}$) for the unstable longitudinal ω_0 and ω_1 modes of the $Re = 500$ KH wave at the key time (5). The results shown here at the truncation levels $N = 11$ and 15 for a spanwise wavenumber $d = 3.6$ should be compared with those for $N = 19$ shown in figure 4. The box in the upper-right corner of each frame shows the nodal spacing of the highest-order Galerkin basis functions corresponding to $\lambda_{\max} = \frac{1}{2}(N-1)$ and $\nu_{\max} = N$.

eigenfunctions for this mode are well resolved at $N = 19$, the eigenvalues at $N = 19$ are probably not as inaccurate as figure 6(*c*) would suggest. The occasional lack of monotonicity in the convergence of Galerkin methods is well known.

These comparisons indicate that the truncation level $N = 19$ is the minimum required to ensure an adequate representation of the eigenfunctions and eigenvalues. Although it might be desirable to have results at a slightly higher truncation level than $N = 19$, we note that the eigenvalues and eigenfunctions are also limited in accuracy by the fact that the KH wave whose stability is being tested is not in a steady state. We shall demonstrate shortly that the eigenvalues and eigenfunctions vary considerably as the background KH wave evolves. Thus the infinitesimal disturbances do not strictly exhibit the exponential time dependence assumed in the derivation of (3.18)–(3.23). The important point is that the results obtained at truncation level $N = 19$ are sufficient for the purposes at hand, namely to demonstrate that secondary instabilities do exist and to determine the dynamical origins of these instabilities.

In the derivation of the stability equations (3.18)–(3.23) we assumed, without *a priori* justification, that the secondary instabilities would have growth rates much larger than any corresponding measure of the temporal variations in the background

KH flow. We may take as an appropriate measure of the fluctuations in the KH fields the 'growth rate' based on the KH wave kinetic energy K', namely

$$\sigma_{\mathrm{KH}} = \frac{1}{2K'}\frac{\mathrm{d}K'}{\mathrm{d}t}. \tag{5.2}$$

Thus an eigenvalue and its corresponding eigenvector are a valid respresentation of one of the genuine unstable modes of the KH flow only if

$$\sigma_{\mathrm{R}} \gg \sigma_{\mathrm{KH}}. \tag{5.3}$$

Since the KH wave never achieves a steady state, the growth rate, frequency and eigenfunction computed for a particular mode must vary as the KH wave evolves. Thus the comparison between the growth rates of the unstable modes and the KH wave should be made at each point in the evolution of the KH wave.

We have recorded in figure 8 the temporal variations of the growth rates σ_{R} for each of the modes identified previously as ω_0, ω_1, ω_2, ω_3 and ω_4, together with the instantaneous growth rate σ_{KH} of the KH wave. The wavenumber for the secondary unstable modes was fixed at $d = 3.6$ because this value is very near the wavenumber corresponding to maximum growth for each of these branches. The sequence of modes with fundamental frequency $\omega_1' = \pm 0.26$ has not been included in figure 8 because the fastest-growing modes in this sequence have wavenumbers significantly smaller than $d = 3.6$. Note that, although the growth rates shown in figure 8 vary considerably as the nonlinear KH wave evolves, the frequencies of the oscillatory modes do not (Klaassen 1982).

Within the accuracy of our analysis, the first appearance of the secondary instability coincides with the emergence of the superadiabatic region in the background KH flow, i.e. shortly before the key time labelled (2*). The KH wave is still growing rapidly at this time, so the growth rates of the unstable modes are not large compared to that of the nonlinear KH wave. Since the criterion (5.3) is not well satisfied, the nature of the early stages of these secondary modes (and in particular the precise moment at which the KH flow first becomes unstable) cannot be accurately determined by the current method. As the evolution of the KH wave proceeds beyond the key time (2*), however, the growth rates of the unstable modes ω_0, ω_1, ω_2 and ω_3 increase rapidly, while the growth rate of the nonlinear KH wave diminishes. By the time the secondary modes achieve their maximum growth rate, the KH wave has achieved its maximum wave kinetic energy (key time (4)), and has begun the slow amplitude oscillations characteristic of the energy cycle. At this time, the criterion (5.3) is easily satisfied. It should be noted, however, that the growth rates of the unstable modes decrease sharply after the maximum value is attained, and apparently vanish altogether before the second occurrence of zero net KH-wave Reynolds stress at the key time (7).

Further insight into the behaviour of these unstable modes may be gained by examining the variation of the eigenfunctions as the background KH flow evolves. Figure 9 shows contour plots of the vertical heat-flux correlations for the unstable modes ω_0, ω_1 and ω_2 with wavenumber $d = 3.6$ at the key points (2*), (3), (4) and (5) in the energy cycle of the nonlinear KH wave. One can see from this figure that the ω_0, ω_1 and ω_2 modes correspond to convective activity that is strongly correlated with the evolving primary superadiabatic region of the nonlinear KH wave. Even at the key time (2*), when the current method of analysis is questionable owing to the violation of (5.3), the eigenfunctions reveal a small region of convective activity coincident with the emerging oval-shaped primary superadiabatic region. As the

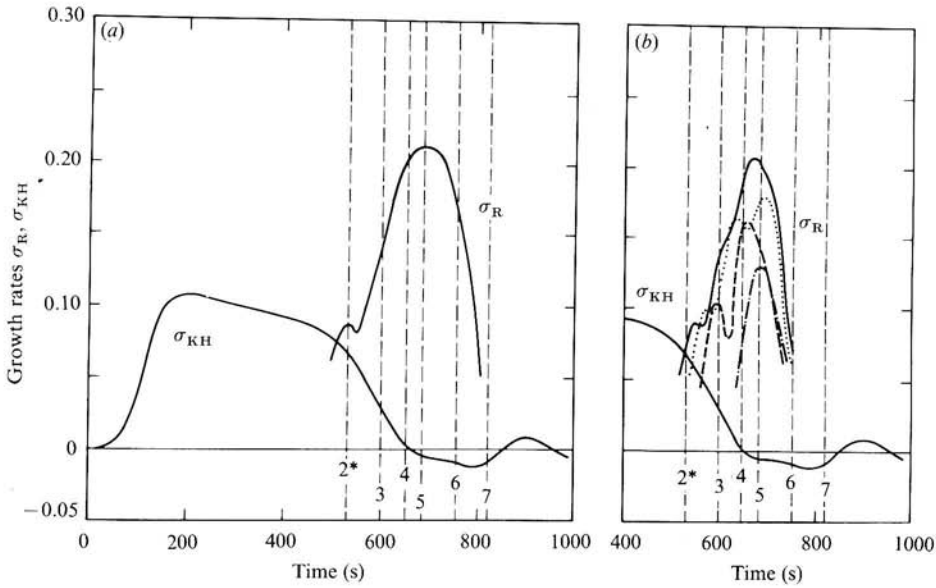

FIGURE 8. Time dependence of the non-dimensional growth rates σ_R of the non-oscillatory (*a*) and oscillatory (*b*) longitudinal modes of the $Re = 500$ KH wave (with spanwise wavenumber $d = 3.6$ and truncation level $N = 19$). Note that the time axis is in units of seconds. The instantaneous growth rate σ_{KH} of the KH wave provides an indication of the magnitude of temporal variations in the nonlinear wave. The vertical dashed lines indicate the key times in the energy cycle of the KH wave. Key for the oscillatory modes: ——, ω_1; · · · ·, ω_2; - - - -, ω_3; –·–, ω_4.

KH wave grows in amplitude, the primary superadiabatic region expands, developing into a ring-shaped area by the time the KH wave achieves its maximum net Reynolds stress (key point (3)). At this time the heat flux of the unstable modes has taken on the same ring-like shape. As the KH wave evolves through the key points (4) and (5) the primary superadiabatic ring and the coincident ring of convective activity spread outward.

The eigenfunctions at the key time (6) in the KH wave energy cycle have not been included in this sequence because they are not well resolved. It can be seen from figure 1 that the outer superadiabatic ring at the key time (6) is much narrower than that at (4) or (5), and is apparently at the limits of resolution imposed by the maximum truncation level $N = 19$. By the time the KH wave has reached the key time (7), the outer superadiabatic region has become extremely narrow, and is on the verge of disappearing altogether.

It is evident from the preceding discussion that the growth of infinitesimal disturbances is strongly modified by the evolving nonlinear KH wave and, contrary to the assumption (3.17), is not purely exponential. Although the criterion that σ_R be much larger than σ_{KH} is a necessary condition for a physically meaningful mode, it is therefore not a sufficient one. Unless the growth rate of a particular mode is sustained for a sufficient length of time during the evolution of the nonlinear KH wave, a small initial disturbance will not be able to grow to finite amplitude. We must therefore develop some means of assessing the potential for the growth of an 'infinitesimal' disturbance based on the temporal variation of its growth rate. If a growth rate σ_R is maintained for a short period of time denoted by Δt, the disturbance would be amplified by a factor equal to $e^{\sigma_R \Delta t}$. If σ_R is a continuous function of time

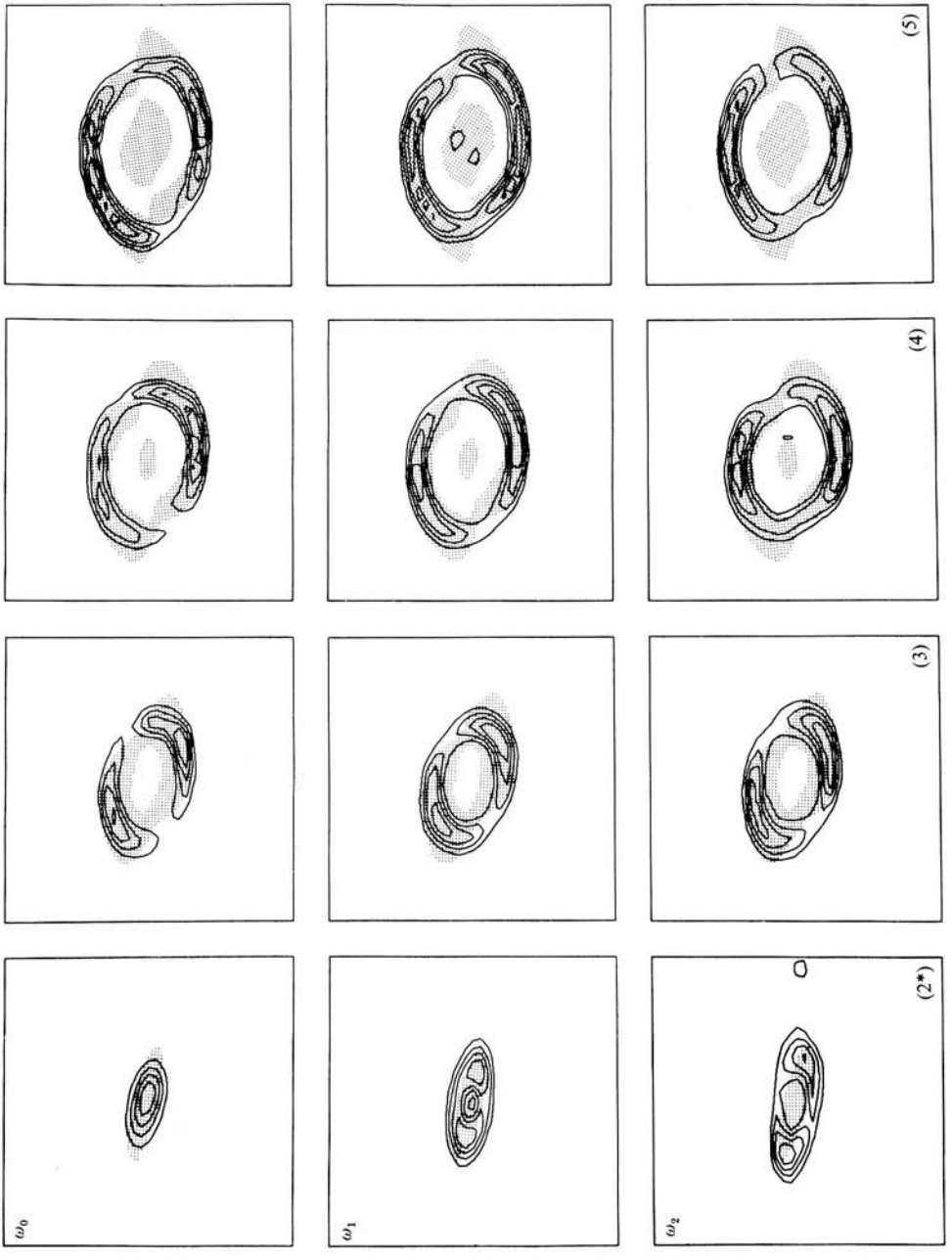

FIGURE 9. Vertical heat-flux correlations ($\overline{\theta' u_z'}^y$) for the longitudinal ($b = 0$, $d = 3.6$) ω_0, ω_1 and ω_2 modes at the key times (2*), ..., (5) in the evolution of the $Re = 500$ KH wave. Note that these modes are all associated with convective activity in the evolving primary SAR of this wave. (The shaded region delineates the evolving primary and secondary SARs.)

t over the interval $0 \leqslant t \leqslant T$ then the total amplification A of the disturbance may be approximated by dividing the interval T into N equal portions of length $\Delta t = T/N$ and taking the product of the amplification factors from each subinterval Δt, i.e.

$$A \approx \prod_{m=1,\,N} \mathrm{e}^{\sigma_{\mathrm{R}m}\,\Delta t} = \exp\left(\sum_{m=1}^{N} \sigma_{\mathrm{R}m}\,\Delta t\right) \approx \mathrm{e}^{\bar{\sigma}_{\mathrm{R}}\,T}, \tag{5.4}$$

where

$$\bar{\sigma}_{\mathrm{R}} \approx \frac{1}{N} \sum_{m=1}^{N} \sigma_{\mathrm{R}m}. \tag{5.5}$$

Taking the limit as $N \to \infty$ or $\Delta t \to 0$,

$$\lim_{\substack{\Delta t \to 0 \\ N \to \infty}} \sum_{m=1}^{N} \sigma_{\mathrm{R}m}\,\Delta t = \int_0^T \sigma_{\mathrm{R}}(t)\,\mathrm{d}t. \tag{5.6}$$

By putting

$$\bar{\sigma}_{\mathrm{R}} = \frac{1}{T} \int_0^T \sigma_{\mathrm{R}}(t)\,\mathrm{d}t, \tag{5.7}$$

we see that the amplification factor

$$A = \mathrm{e}^{\bar{\sigma}_{\mathrm{R}}\,T} \tag{5.8}$$

over the time interval T is related to the area under the curve of σ_{R} versus t.

Using the data in figure 8, we have computed the amplification factors $\mathrm{e}^{\bar{\sigma}_{\mathrm{R}}\,T}$ for each of the modes ω_0, ω_1, ω_2, ω_3 and ω_4, and compiled the results in table 2. For purposes of comparison, we have also calculated the amplification factor for the primary KH instability based on the value of σ_{KH} calculated from the data in KP. It should be emphasized that the amplification factors computed here are intended only as crude measures of the *potential* a particular mode has to achieve finite amplitude. We have not included the uncertain growth rates near the key point (2*) (where the requirement (5.3) breaks down) in the computation of these factors, and the accuracy of the growth rates near and beyond the key point (6) is questionable. Furthermore, the true time dependence of unstable modes evolving in a KH wave is not likely to be given by the function $\mathrm{e}^{\sigma t}$, where σ is the time-varying eigenvalue computed by our approximate method of stability analysis. In fact the actual amplification experienced by the $Re = 500$ KH billow is equal to 9700 (based on the increase in the square root of the wave kinetic enegy in the linear regime) rather than the value 7120 predicted in table 2. Taking all these caveats into consideration, it still seems likely that the non-oscillatory mode ω_0, which according to table 2 has an amplification factor nearly seven times that of its nearest competitor ω_1, will be the dominant unstable mode. However, the amplification factor of the ω_1 mode is large enough that we cannot exclude the possibility of its being simultaneously amplified. We should also point out that the ω_1 mode displayed a lesser degree of convergence than the ω_0 mode, indicating a greater degree of uncertainty in the ω_1 mode's amplification factor. Because the spatial structure of the ω_0 and ω_1 modes is very similar, there is also a distinct possibility that, once 'finite' amplitude has been attained, nonlinear interactions could enhance the growth of the ω_1 mode. While the fate of the ω_2 mode is similarly uncertain, it seems unlikely that the ω_3 or ω_4 modes will ever achieve finite amplitude of their own accord.

We turn our attention to the question of the effect that the evolving nonlinear KH wave has on the various unstable branches in wavenumber space. Figure 10 illustrates the wavenumber dependence of the branches corresponding to ω_0, ω_1 and ω_2 at the key points (3), (4), (5) and (6) in the energy cycle of the KH wave. Note that, for each of these branches, all but the longest-wavelength modes achieve their maximum

Truncation level: N	Angular frequency $\lvert\omega_1\rvert$	$\lvert\omega_2\rvert$	$\lvert\omega_3\rvert$	$\lvert\omega_4\rvert$	$\lvert\omega_1'\rvert$	$\lvert\omega_2'\rvert$
7	0.13	0.28	—	—	—	—
11	0.12	0.35	—	—	0.22	—
15	0.13	0.35	0.48	0.61	0.24	—
19	0.17	0.33	0.54	0.70	0.26	0.49

TABLE 1. Angular frequency of the various longitudinal modes of instability as a function of the truncation level. The dashes indicate that a particular mode was not identifiable at the truncation level in question.

Mode	ω_0	ω_1	ω_2	ω_3	ω_4	KH
Initial time t_i (s)	574.5	574.5	574.5	547.5	643.1	17.15
Final time t_f (s)	797.5	763.2	763.2	728.9	746.0	651.70
$T = u_0/h(t_f - t_i)$	44.1	37.3	37.3	30.5	20.3	125.70
$\overline{\sigma_R}$	0.174	0.154	0.136	0.121	0.104	0.071
$\overline{\sigma_R}T$	7.69	5.75	5.08	3.68	2.12	8.87
$e^{\overline{\sigma_R}T}$	2190	314	160	40	8	7120

TABLE 2. Amplification factors $e^{\overline{\sigma_R}T}$ for the modes in the sequence with fundamental frequency $|\omega_1| \approx 0.17$ at the wavenumber $d = 3.6$. The integrations required for $\overline{\sigma_R}T$ were performed over a time interval extending from just before the key point (3) to just beyond the key point (6), i.e. from $t_i = 574.5$ s to $t_f = 797.5$ s. If σ_R vanished on this interval the shorter interval indicated in the table was used. Note that the unit of nondimensional time is $h/u_0 = 5.054$ s.

growth near the key point (5). Also note that all growth rates belonging to a particular branch, with the exception of those at the longest wavelengths, rise uniformly before the maximum at the key time (5) and decline uniformly thereafter. This figure also shows that the wavenumber of the fastest-growing mode of a particular branch increases significantly with time before the key time (5) and then decreases only slightly thereafter. In table 3 we have compiled the wavenumbers of the fastest-growing modes for each of the branches ω_0, ω_1 and ω_2 at the key times (3), (4), (5) and (6).

We have thus far neglected the effect of the evolving nonlinear KH wave on the sequence of unstable modes that were found to be associated with the secondary (inner, oval-shaped) superadiabatic region at the key time (5), i.e. the sequence of modes with fundamental frequency $|\omega_1'| = 0.26$. Heat-flux correlations (not shown here) indicate that this association persists as the KH wave evolves and the secondary SAR expands outward into a ring-shaped region. Figure 11 depicts the shape of the ω_0' and ω_1' branches in wavenumber space at the key points (5), (6) and (7). These modes clearly never achieve the large growth rates typical of the sequence of modes with fundamental frequency $|\omega_1| = 0.17$. Amplification factors for the ω_1' sequence never exceed values of $e^{\overline{\sigma}_R T} \sim 60$, indicating that such disturbances do not have much intrinsic potential for achieving finite amplitude. This is consistent with the analysis described in §2, which showed that the Rayleigh number associated with the secondary SAR is generally lower than the corresponding Rayleigh number of the primary SAR. It appears that the unstable modes associated with the emergence of the first SAR will reach finite amplitude and significantly alter the nonlinear

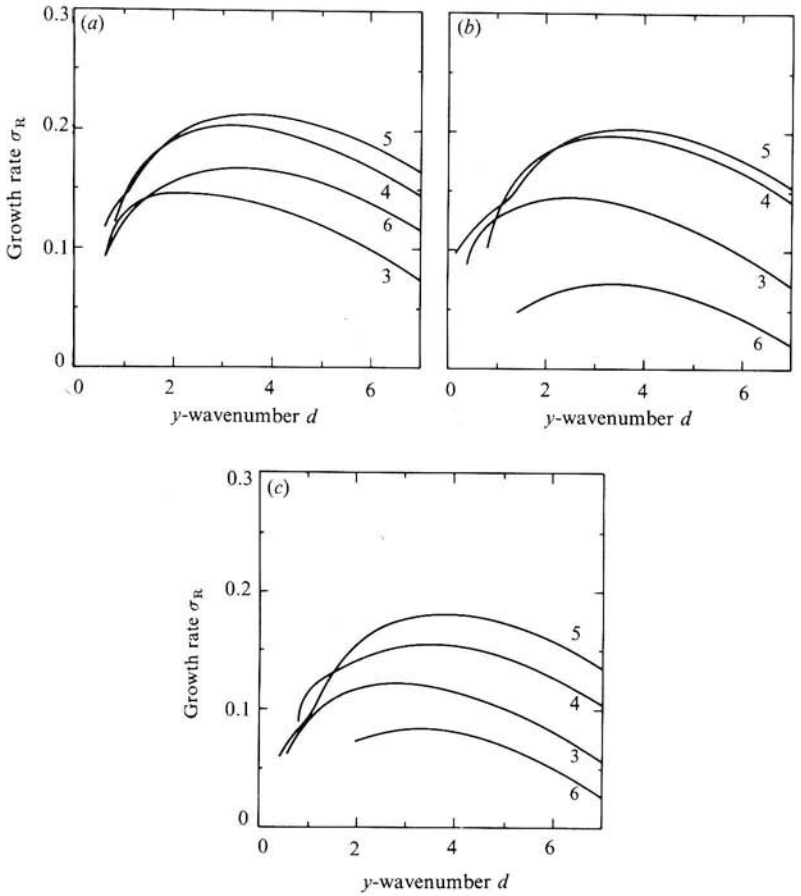

FIGURE 10. Growth rate σ_R of the ω_0 (*a*), ω_1 (*b*) and ω_2 (*c*) longitudinal modes as a function of the spanwise wavenumber d for the $Re = 500$ KH wave at the key times (3), ..., (6) in its energy cycle. (Curves are labelled according to the key time.)

(*a*)

Key time	ω_0	ω_1	ω_2	ω_0'	ω_1'
(3)	2.3	2.4	2.9	—	—
(4)	3.2	3.4	3.5	—	—
(5)	3.6	3.6	3.8	1.0	1.3
(6)	3.4	3.4	3.3	1.4	2.0
(7)	—	—	—	1.8	1.3

(*b*)

Key time	ω_0	ω_1	ω_2	ω_0'	ω_1'
(3)	0.147	0.145	0.122	—	—
(4)	0.204	0.197	0.156	—	—
(5)	0.213	0.202	0.181	0.098	0.109
(6)	0.169	0.072	0.083	0.105	0.105
(7)	—	—	—	0.101	0.103

TABLE 3. (*a*) Wavenumbers d of the fastest-growing modes with frequencies ω_0, ω_1, ω_2, ω_0' and ω_1' at the key times (3), (4), (5), (6) and (7) in the KH wave energy cycle. (*b*) Growth rates σ_R of the same fastest-growing modes.

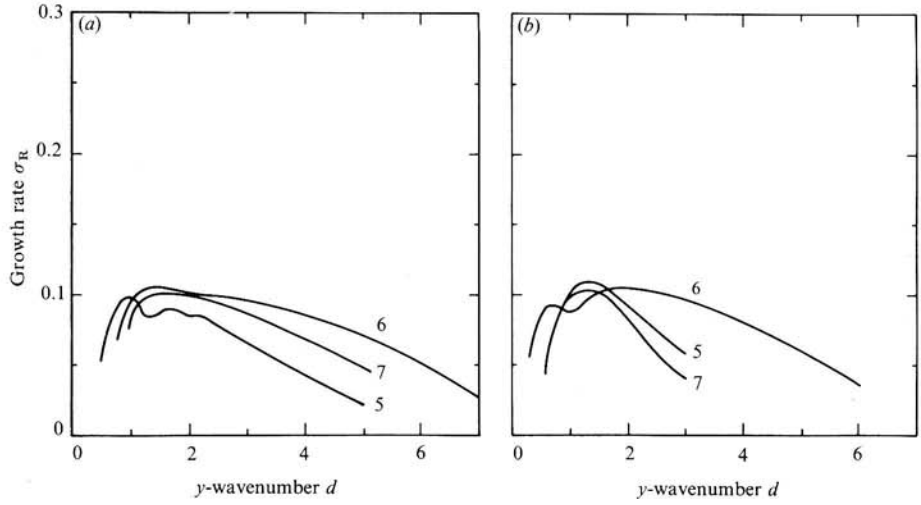

FIGURE 11. Growth rate σ_R of the ω_0' (*a*) and ω_1' (*b*) longitudinal modes as a function of the spanwise wavenumber d for the $Re = 500$ KH wave at the key times (5), ..., (7) in its energy cycle. (Curves are labelled according to the key time.)

evolution of the wave before the modes associated with the secondary SAR have an opportunity to achieve any significant growth. In the remainder of this paper we therefore consider only those unstable modes associated with the primary SAR.

6. The Reynolds-number dependence of secondary instabilities with longitudinal symmetry

We begin with a comparison of the unstable modes of the Kelvin–Helmholtz waves at $Re = 300$ and $Re = 900$. A prior search of wavenumber space has revealed that the most-unstable modes of the $Re = 300$ KH wave occur at wavenumbers near $d = 1.7$, while those for the $Re = 900$ KH wave occur near $d = 4.7$. We therefore use these fixed wavenumbers for the purpose of displaying in figure 12 the temporal evolution of the growth rate σ_R for each of the ω_0, ω_1 and ω_2 modes of the $Re = 300$ and $Re = 900$ KH waves. We have also included in this figure the growth rates σ_{KH} of the corresponding nonlinear KH waves. The maximum growth rates of the ω_0, ω_1 and ω_2 modes at $Re = 900$ are much larger than those of the corresponding modes at either $Re = 300$ or $Re = 500$ (figure 8), and easily satisfy the criterion $\sigma_R \gg \sigma_{KH}$. Note that, while the $Re = 900$ and $Re = 500$ KH waves are most unstable between the key times (4) and (5), the $Re = 300$ wave is most unstable between the key times (3) and (4). In fact, by the time the key point (5*a*) (zero KH wave Reynolds stress) is attained by the $Re = 300$ billow, the unstable modes have been considerably damped. This marked difference in behaviour, which can be attributed to the increased importance of thermal and viscous diffusion at low Reynolds numbers, forces us to introduce the key points (2*) and (3*) at $t = 651.70$ and 754.60 s respectively in the evolution of the $Re = 300$ KH wave. The maximum growth rates of the ω_0, ω_1 and ω_2 modes at $Re = 300$, which occur near the key time (3*), are considerably smaller than those of the corresponding modes at either $Re = 500$ or $Re = 900$. In fact these maximum growth rates are only about four times larger than the growth rate σ_{KH} of the $Re = 300$ KH wave at (3*), causing some degree of

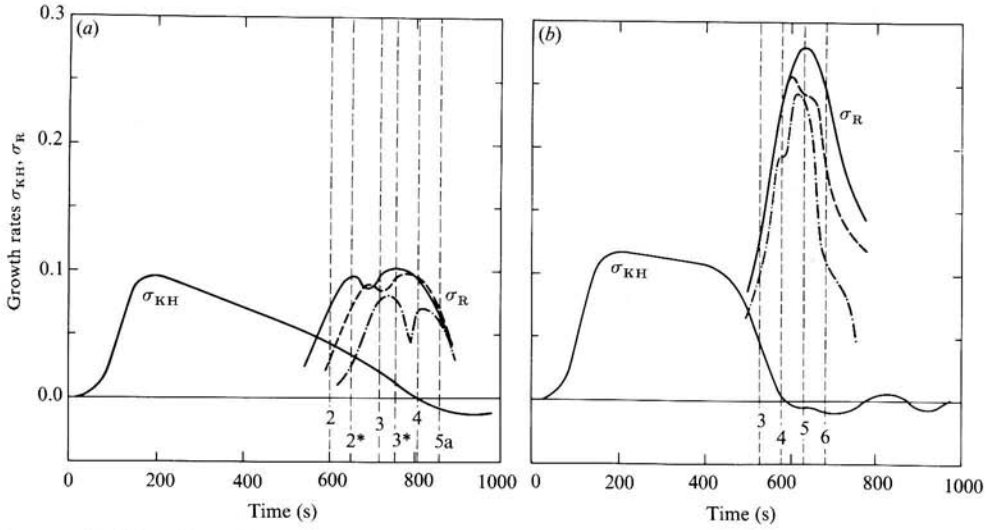

FIGURE 12. Time dependence of the non-dimensional growth rates σ_R of the unstable ω_0 (——), ω_1 (- - - -) and ω_2 (—·—) longitudinal modes of the $Re = 300$ (*a*) and $Re = 900$ (*b*) KH waves. The instantaneous growth rates σ_{KH} of the KH waves provide an indication of the magnitude of the temporal variations in the nonlinear waves. The vertical dashed lines indicate the key times in the energy cycles of the KH waves. Note that the spanwise wavenumber was fixed at $d = 1.7$ in the case of $Re = 300$ and at $d = 4.7$ for the $Re = 900$ wave. The ω_3 and ω_4 modes were excluded for the sake of clarity.

uncertainty in their accuracy. However, the important fact is that the growth rates of the unstable modes display the general trend of decreasing sharply as the Reynolds number is decreased. This behaviour suggests the existence of a critical Reynolds number, below which the two-dimensional KH billow is stable. The problem of estimating this critical value of the Reynolds number will be considered later in this section.

Figure 13 shows the wavenumber structure of the branches $\omega_0, \ldots, \omega_4$ at a time when each of these modes is near maximum growth (i.e. at the key point (3*) in the case of $Re = 300$ and at the key point (5) in the case of $Re = 900$). Apparently the growth rates of the ω_4 mode at $Re = 300$ are too small to be revealed by the current method. In figure 14 we compare the evolution of the heat-flux correlations for the ω_0 modes of the $Re = 300$ and 900 KH waves. The disturbance heat flux is, as it was for the $Re = 500$ wave, everywhere positive and remains well correlated with the expanding primary SARs of both KH waves.

We have also analysed the stability of the KH waves generated by our nonlinear numerical model at $Re = 400$ and $Re = 700$. The most-unstable modes at $Re = 400$ were found to occur near the key time (4), while those at $Re = 700$ occurred near the key time (5). In an attempt to obtain some information about the inviscid limit, we removed all of the diffusive terms from the stability equations (3.18)–(3.23) and used the $Re = 900$ KH wave state at the key point (5) as an approximation to the most-unstable inviscid KH wave state. The most-unstable branches corresponding to the modes ω_0, ω_1 and ω_2 have been compiled in figure 15 for various KH waves with Reynolds numbers in the range $300 \leqslant Re \leqslant 900$. It is important to note that, for each of these simulations, the growth of the primary KH wave was induced in precisely the same way, i.e. according to scheme A of KP. Thus the simulations may be compared without considering the sensitivity of KH wave character to the

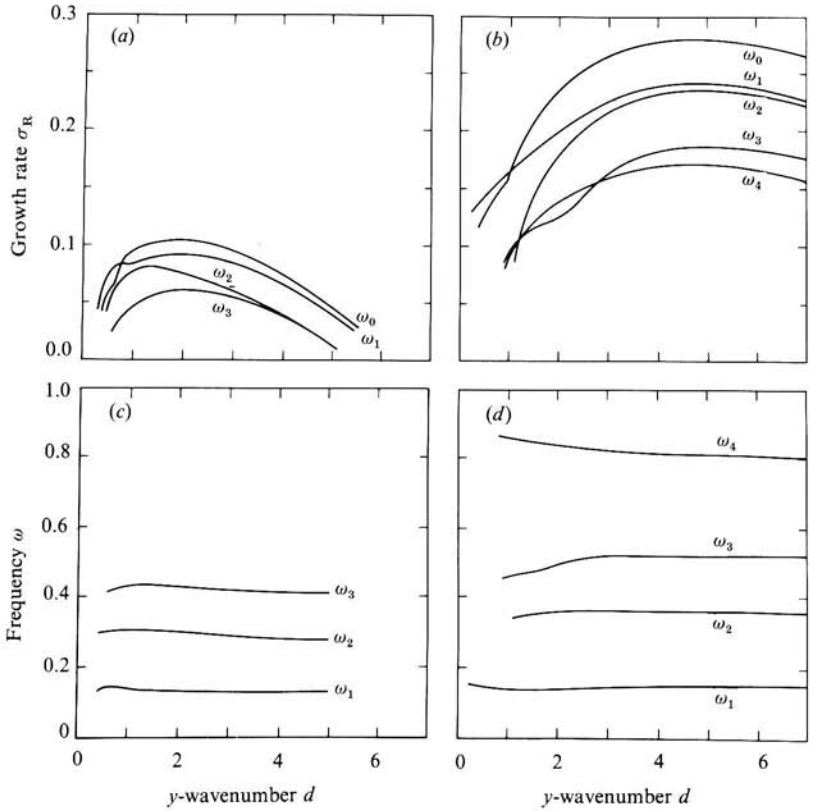

FIGURE 13. A comparison of the growth rates σ_R and frequencies ω of various unstable longitudinal modes of the $Re = 300$ KH wave at the key time (3*) with the corresponding modes of the $Re = 900$ KH wave at the key time (5): (*a*) σ_R ($Re = 300$), (*b*) σ_R ($Re = 900$), (*c*) ω ($Re = 300$) and (*d*) ω ($Re = 900$) as functions of the spanwise wavenumber d. Note that the growth rate of the ω_4 mode at $Re = 300$ is apparently too small for it to be revealed by the current method.

amplitude and structure of the disturbance that induces wave growth. This sensitivity will be discussed in more detail later in this section.

We have superimposed on figure 15 the growth rate of the invisid primary Kelvin–Helmholtz instability as a function of the wavenumber. (Note that the wave vector of the primary KH instability is orthogonal to the wave vector of the secondary mode of instability.) The fastest-growing secondary modes have wavelengths that are considerably shorter than the fastest-growing modes of the primary KH instability. For example the fastest-growing ω_0 mode at $Re = 500$ (key point (5)) has wavenumber $d = 3.6$, which corresponds to a wavelength $D = 2\pi/d = 0.87$, while the KH wavelength is given by $L \approx 16$ (both in units of h). The aspect ratio of the convection 'rolls' is given by

$$\frac{D}{2\,\delta/h} \approx 0.7,$$

where $\delta = 0.65h$ is the depth of the corresponding superadiabatic region at $x = \frac{1}{2}L$. A factor of two has been included because each wavelength in the y direction contains two convective cells. The cross-sections of the convection 'rolls' are therefore slightly elliptical, with their major axis in the vertical direction. It is clear that the spanwise

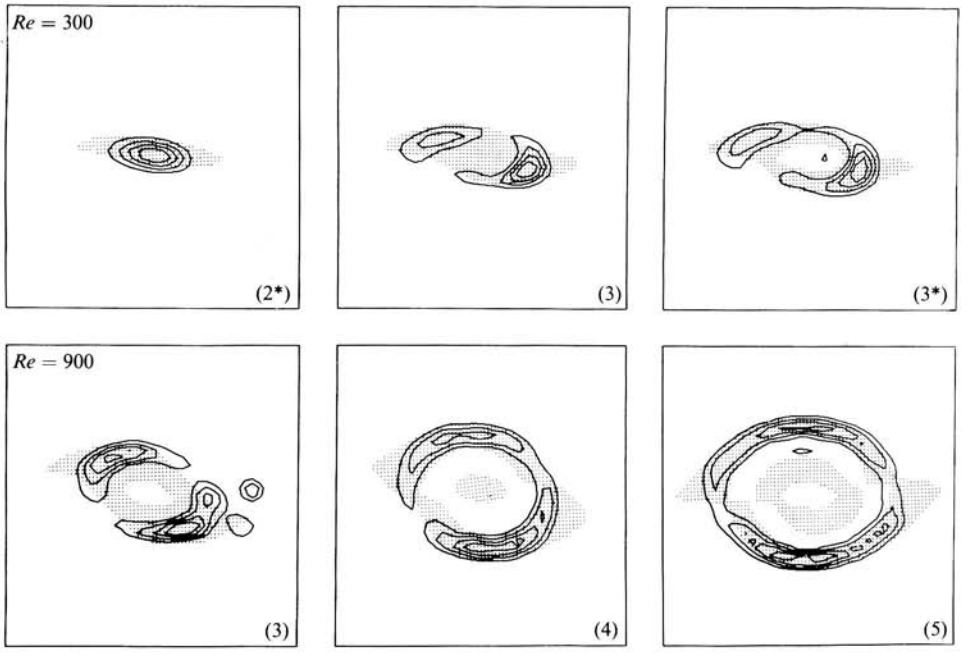

FIGURE 14. Evolution of the vertical heat-flux correlations ($\overline{\theta' u_z'}^y$) for the longitudinal ω_0 modes of the $Re = 300$ and 900 KH waves. The spanwise wavenumber $d = 1.7$ for $Re = 300$, while $d = 4.7$ for $Re = 900$. The key times are indicated in the lower-right corner of each frame. Note the correlation of the convective activity (positive heat flux) with the primary portion of the (shaded) SAR.

scale of the most-unstable secondary modes is determined by the depth of the superadiabatic region.

Figure 15 also shows a marked disparity in bandwidth between the primary KH and secondary unstable modes. As a consequence of the narrow bandwidth of the primary KH instability, the subharmonics and higher harmonics of the fastest-growing KH mode do not interact strongly with the mean flow, and can only be significantly amplified after the fundamental mode has reached finite amplitude. This results in a nonlinear wave whose spectrum is dominated by the fundamental harmonic, at least until subharmonic instabilities set in. (The process of vortex pairing associated with subharmonic amplification will be described elsewhere.) On the other hand, the extremely broad bandwidth of the secondary instabilities could permit both subharmonics and higher harmonics of the fastest-growing mode to be significantly amplified at the same time as the fundamental mode. For example the fastest-growing mode on the ω_0 branch at $Re = 700$ occurs at the wavenumber $d \approx 4.1$, and the growth rates of the first subharmonic and second harmonic of this mode are only reduced by about 15 % from maximum value. Furthermore, the fastest-growing modes of the ω_1 and ω_2 branches at $Re = 700$ also have growth rates that are not more than 15 % lower than that of the fastest-growing ω_0 mode. If such a variety of modes with differing spatial structure and temporal behaviour were simultaneously amplified, the disorder of the flow would certainly be increased. At the present time we may only conjecture as to how this disorder would be manifested. It is possible that the disorder could simply appear as spatial or temporal inhomogeneities in a laminar pattern of

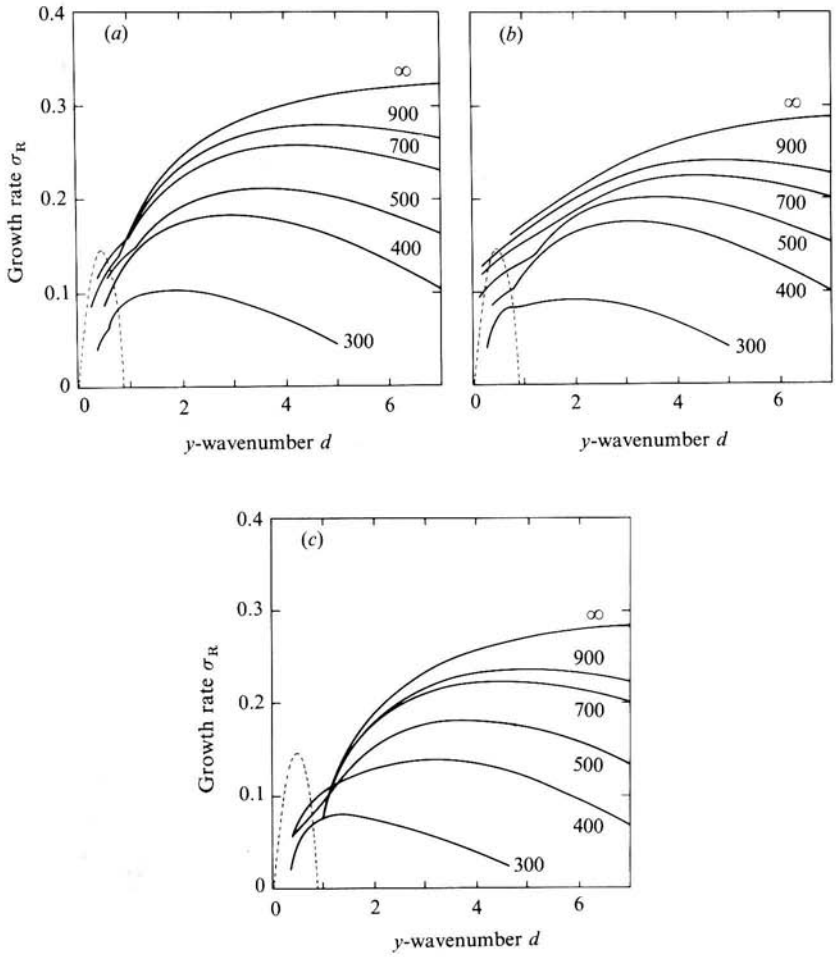

FIGURE 15. A comparison of the fastest-growing ω_0 (*a*), ω_1 (*b*) and ω_2 (*c*) branches for KH waves with various Reynolds numbers (see labels on each curve). The $Re = 300$ and 400 branches are shown at the key times (3*) and (4) respectively, while for all other Re the branches are shown at the key time (5). The broad bandwidth of these secondary longitudinal modes may be contrasted with the extremely narrow bandwidth of the inviscid primary KH mode (dashed curve). Note that the KH mode is transverse.

convection rolls. However, it is equally likely that nonlinear interactions between the amplified modes could lead to the onset of turbulence.

Another interesting feature of figure 15 is that the bandwidth of each of the unstable modes ω_0, ω_1 and ω_2 increases as the Reynolds number increases. In fact, the bandwidth for our approximation to the inviscid case appears to be infinite. This feature, in which the most-unstable modes in the absence of thermal and viscous diffusion are those with the shortest wavelength, is a common property of convective instabilities. The growth rates of instabilities having dynamical origins (such as the primary KH instability) tend to be limited at small wavelengths by dynamical rather than diffusive processes, so that their bandwidth is restricted even in the inviscid limit.

We have calculated the growth rate, wavenumber and frequency of the fastest-growing mode for each of the branches displayed in figure 15 and plotted them as

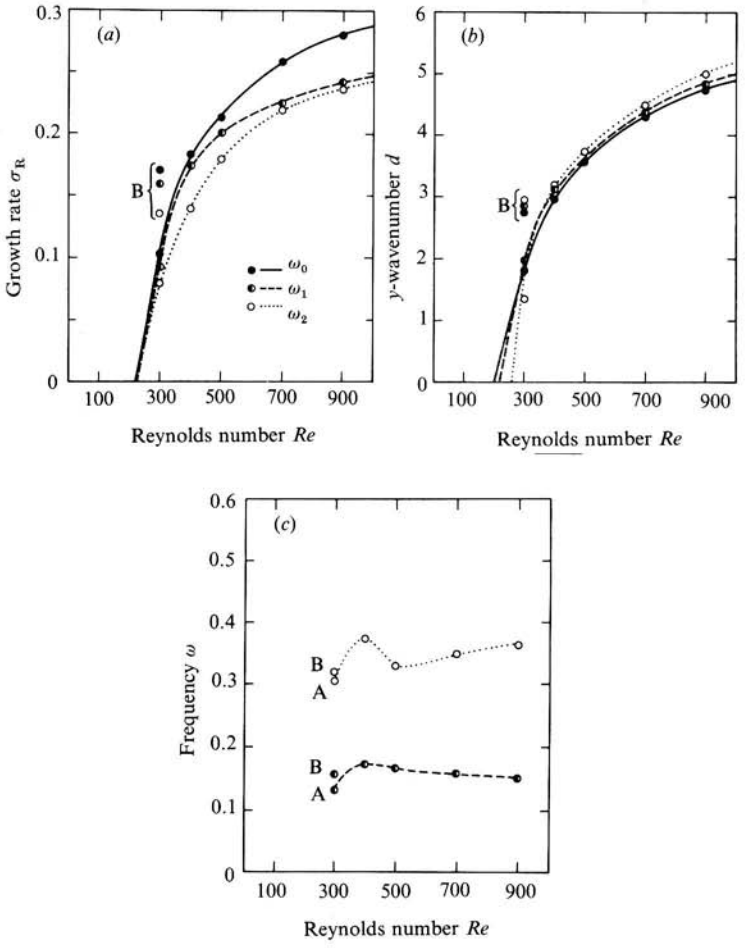

FIGURE 16. (*a*) Growth rate σ_R, (*b*) wavenumber d, and (*c*) frequency ω of the fastest-growing longitudinal ω_0, ω_1 and ω_2 modes as functions of the Reynolds number. Note the sharp onset of all three modes of instability in the neighbourhood of $Re \approx 220$. The dotted, dashed and solid curves represent data obtained from KH waves initialized according to scheme A. The data obtained from the $Re = 300$ scheme-B simulation has been labelled with a B.

a function of the Reynolds number in figure 16(*a*). Again we remind the reader that this comparison is valid only because each KH wave simulation was initialized in precisely the same way. If we bear in mind that the accuracy of the growth rates at $Re = 300$ is somewhat uncertain, we may extrapolate the curves of σ_R versus Re in figure 16(*a*) to locate the critical Reynolds number Re_c for the transition of two-dimensional KH waves to a fully three-dimensional flow. This procedure yields a value of $Re_c \approx 220 \pm 50$ for each of the three modes ω_0, ω_1 and ω_2. The shapes of the σ_R versus Re curves also suggest that the growth rates are approaching a limiting value as $Re \to \infty$. This provides an *ad hoc* justification for the approximations made in obtaining the inviscid growth rates presented in figure 15. Also note that the dominance of the ω_0 mode over the ω_1 and ω_2 modes increases with increasing Reynolds number in the interval $400 \leqslant Re \leqslant 900$, while the growth rates of the latter two modes converge as the Reynolds number increases in the same interval.

The values of the critical Reynolds number obtained from the σ_R versus Re curves

may be corroborated with the aid of the corresponding d versus Re curves in figure 16(*b*). The graph shows that the wavenumbers of the fastest-growing ω_0, ω_1 and ω_2 modes all decrease sharply as the Reynolds number decreases. Assuming the neutrally stable modes to have infinite wavelengths, we find by extrapolation that the critical Reynolds number is again near $Re_c \approx 220 \pm 50$. This value for the critical Reynolds number is consistent with our earlier prediction (based on the Rayleigh numbers computed in §2) that the nonlinear Kelvin–Helmholtz billow should be marginally unstable at $Re = 300$. The reader should also note the striking resemblance between figures 2 and 16(*a*), which suggests that the Rayleigh number Ra^* provides a good measure of the stability of the KH wave.

In contrast with the behaviour of σ_R and d, the frequencies ω of the fastest-growing modes in figure 16(*c*) show remarkably little variation with the Reynolds number. Considering the vastly different character of the KH waves at $Re = 300$ and $Re = 900$, this result is somewhat unexpected. The mean value for the angular frequency of the ω_1 mode is about 0.16 in non-dimensional units, while that for the ω_2 mode is about 0.34. These two angular frequencies correspond to periods $T_1 \approx 200$ s and $T_2 \approx 94$ s respectively for the choice of scales employed in KP. The period of the energy cycle of the nonlinear KH wave, $T \sim 290$ s, was found in KP to correspond to the orbital period of a fluid particle about the central vortex. However, it is clear that the fundamental period T_1 cannot correspond to an orbital period of a fluid particle about, for example, a convection roll. First we have a Fourier spectrum of modes to explain, and secondly the amplitude of the disturbance is arbitrary.

The shape of the loci of σ_R verses Re in figure 16(*a*) implies that there is a sharp demarcation between KH waves that are unstable and those that are not. However, this is somewhat misleading. According to the results obtained in KP, the critical Reynolds number we have obtained ($Re_c \approx 220$) is in the regime where the nonlinear characteristics of KH waves are very sensitive to the amplitude and structure of the disturbance that induces wave growth. This sensitivity arises from the diffusion of the mean flow which occurs prior to the onset of nonlinear wave–mean-flow interactions. Thus the loci of σ_R versus Re and the critical Reynolds number shown in figure 16(*a*) apply only to KH waves that are initialized according to scheme A of KP. We tested the sensitivity of KH waves with $Re = 300$ to the nature of their initialization by performing an additional simulation (see KP) in which wave growth was induced by a more energetic disturbance that more closely approximated an unstable eigenmode of the parallel flow. This scheme-B initialization produced a KH wave with a significantly larger maximum amplitude than the scheme-A $Re = 300$ KH wave. Furthermore, the dynamical features of the scheme-B $Re = 300$ KH wave more closely resembled those of the $Re = 500$ KH wave initialized by scheme A.

We have tested the stability of the scheme-B $Re = 300$ KH wave against infinitesimal disturbances with longitudinal symmetry, and have found that the growth rates of the unstable ω_0, ω_1 and ω_2 modes are significantly larger than the corresponding unstable modes of the scheme-A $Re = 300$ KH wave. The most-unstable modes of the scheme-B $Re = 300$ KH wave were found at the key time (5) (zero net KH wave Reynolds stress), and their growth rates, wavenumbers and angular frequencies have been recorded in figure 16. If we were to compute and test the stability of a sequence of scheme-B KH waves with various Reynolds numbers, we would find that the σ_R versus Re curves would be raised slightly at large Re, and the critical Reynolds number would be shifted to a lower value. Although a sharp demarcation between stable and

unstable KH waves exists for a given initialization, the critical Reynolds number also depends on the amplitude and structure of the disturbance that induces wave growth. Thus the concept of a critical Reynolds number is ambiguous for this flow.

7. Conclusions

We have tested two-dimensional finite-amplitude KH waves for stability against three-dimensional infinitesimal disturbances, and have found that they are most unstable against longitudinal modes which correspond to convective activity in the statically unstable regions induced by the roll-up of the nonlinear wave. Estimates of the amplification factors for these longitudinal modes have shown that for high Reynolds numbers the growth rates are maintained at large values for periods of time that should be sufficient to allow the disturbances to achieve large amplitude.

We have shown that the critical Reynolds number for this transition, Re_c, lies in the regime in which the nonlinear KH wave characteristics and thus Re_c itself are sensitive to the amplitude and structure of the disturbance which induces KH wave growth. This result is consistent with observations by Woods (1969), who reported a value of $Re_c \sim 100$ (in our choice of scales) for the onset of turbulence in KH waves developing in the oceanic thermocline. We should note that the observations are for $Pr \sim 10$ and that Woods failed to specify values of the initial minimum Richardson number. Further support is provided by the experiments of Koop & Browand (1979), who have observed the onset of turbulence in a KH wave developing in a saline flow for which $Re = 75$, $Ri = 0.075$ and $Pr \approx 700$.

Thorpe (1973) has identified the transition to turbulence in his tilted-tube experiments with the onset of fully three-dimensional small-scale motions in the core of the two-dimensional Kelvin–Helmholtz billow. The turbulent motions gradually spread throughout the shear layer, resulting in the billow's collapse. These observations are consistent with the localized origin and intrinsic three-dimensionality of the unstable longitudinal modes that our theoretical analysis has revealed. We have shown that these modes are confined to the statically unstable regions in the KH wave's core as long as their amplitude remains small. Thorpe also observed that the first appearance of the small-scale structure closely coincides with the time that the billows achieve their maximum amplitude. This is also consistent with our findings which indicate that, while the longitudinal modes achieve their largest growth rates shortly after the billow attains its maximum amplitude, the growth of these instabilities is initiated earlier in the KH wave's evolution. However, we should note that Thorpe was unable to establish whether or not the onset of turbulent motions had a limiting effect on billow growth. Finally, the preferred lengthscales of the instability are consistent with the scale of the turbulence observed in Thorpe's experiments. Although Thorpe did not ascertain the physical origin of the secondary instability observed in his experiments on KH waves, there is little doubt that this instability arises from the buoyancy-driven longitudinal modes revealed by our theoretical analysis. For the region of parameter space investigated, we have found no evidence for a centrifugal instability of the recirculating fluid in the core of the billow. The possibility that secondary KH waves may form on the braids of the primary wave will be examined in a future publication. Within the region of parameter space considered here, however, such disturbances are at most of minor importance.

It is interesting that the longitudinal modes of instability appear to form a discrete

spectrum of oscillatory modes corresponding to the angular frequencies $\omega = 0, \omega_1, 2\omega_1, 3\omega_1$ and $4\omega_1$, with growth rates that generally decrease with increasing frequency. The fundamental frequency of this spectrum, ω_1, is incommensurate with the characteristic frequency associated with the energy cycle in the nonlinear KH wave. Since the growth rate of the fastest-growing mode $\omega = 0$ is not substantially larger than that of the mode with $\omega = \omega_1$, one might be tempted to interpret the instability as a transition to a quasiperiodic flow with only two incommensurate frequencies. This would suggest the picture of the turbulence transition outlined by Ruelle & Takens (1971). However, we must emphasize that this idea is highly conjectural. At the present time we do not know if the fastest-growing mode ($\omega = 0$) will dominate the finite-amplitude disturbance, or whether modes with slightly smaller growth rates (e.g. $\omega = \omega_1$) may also contribute.

Since the observations of Thorpe and others show no intervening bifurcations between the formation of KH waves and the onset of small-scale turbulent motions, one is inclined to directly identify the secondary instability we have discovered with the transition to turbulence. Certainly this instability has, at sufficiently high Reynolds numbers, many of the characteristics one might expect of a turbulence transition. For example, the preferred lengthscales of the unstable modes are small compared with the dominant spatial scales of the nonlinear wave. Furthermore, there exist several unstable modes having distinct frequencies and nearly equal growth rates. The bandwidth of each of these modes is also extremely broad, which indicates that there is no clearly preferred spatial scale. The simultaneous amplification of several modes with distinct spatial and temporal characteristics would lead to complicated and possibly turbulent motions.

However, we must exercise caution here. Although it is clear from the close correspondence with the observations that the instability we have discovered is intimately related to the transition to turbulence in Kelvin–Helmholtz waves, the precise manner in which this transition proceeds remains obscure. A linear analysis such as the one employed in this study provides growth rates for infinitesimal non-interacting modes only. Turbulence, on the other hand, is a highly nonlinear phenomenon for which modal interactions are of crucial importance. Either interactions between disturbances with different temporal characteristics (i.e. modes from different branches in the spectrum) or interactions between disturbances with different spatial characteristics (i.e. modes from a particular broadband branch in the spectrum), or a combination of both types of interactions could lead to the observed chaotic motions. We also cannot exclude the possibility that the unstable longitudinal disturbances may develop into a row of laminar convection rolls with their axes parallel to the mean shear. After achieving some critical amplitude, these rolls could themselves be subject to a further instability, turbulent or otherwise.

At the present time we have no means of determining which of these possibilities is correct. We intend to address this question in the near future by performing three-dimensional fully nonlinear simulations of the evolution of Kelvin–Helmholtz waves. We expect that the results of the present study will provide invaluable guidance in the execution and interpretation of these future analyses.

The National Center for Atmospheric Research (NCAR) in Boulder, Colorado, provided the computer time required for this study. NCAR is sponsored by the National Science Foundation. NCAR's computing facilities were accessed through the University of Toronto remote-job-entry system, which is funded by the Natural Sciences and Engineering Research Council of Canada (NSERC). This research was also supported through NSERC grant A9627.

REFERENCES

Boyd, J. 1978 Spectral and pseudospectral methods for eigenvalue and nonseparable boundary value problems. *Mon. Weather Rev.* **106**, 1192.

Brown, G. L. & Roshko, A. 1974 On density effects and large structure in turbulent mixing layers. *J. Fluid Mech.* **64**, 775.

Busse, F. H. 1972 The oscillatory instability of convection rolls in a low Prandtl number fluid. *J. Fluid Mech.* **52**, 97.

Clever, R. M. & Busse, F. H. 1974 Transition to time-dependent convection. *J. Fluid Mech.* **65**, 625.

Davis, P. A. & Peltier, W. R. 1979 Some characteristics of the Kelvin–Helmholtz and resonant overreflection modes of shear flow instability and of their interaction through vortex pairing. *J. Atmos. Sci.* **36**, 2394.

Denny, V. E. & Clever, R. M. 1974 Comparison of Galerkin and finite difference methods for solving highly nonlinear thermally driven flows. *J. Comp. Phys.* **16**, 271.

Jordan, D. W. & Smith, P. 1977 *Nonlinear Ordinary Differential Equations.* Oxford University Press.

Keller, H. B. 1976 *Numerical Solution of Two Point Boundary Value Problems.* SIAM Regional Conf. Ser. in Appl. Maths, vol. 24. Arrowsmith.

Kelly, R. E. 1977 The onset and development of Rayleigh–Bénard convection in shear flows: a review. In *Physiochemical Hydrodynamics*, vol. 1 (ed. V. G. Levich). Advance.

Klaassen, G. P. 1982 The transition to turbulence in stably stratified parallel flows. Ph.D. thesis, University of Toronto.

Klaassen, G. P. & Peltier, W. R. 1985*a* The evolution of finite amplitude Kelvin–Helmholtz billows in two spatial dimensions. *J. Atmos. Sci.* (in press).

Klaassen, G. P. & Peltier, W. R. 1985*b* The effect of the Prandtl number on the evolution and stability of finite amplitude Kelvin–Helmholtz billows. *Geophys. Astrophys. Fluid Dyn.* (in press).

Koop, C. G. & Browand, F. K. 1979 Instability and turbulence in a stratified fluid with shear. *J. Fluid Mech.* **93**, 135.

Ogura, Y. & Phillips, N. A. 1962 Scale analysis of deep and shallow convection in the atmosphere. *J. Atmos. Sci.* **19**, 173.

Peltier, W. R., Hallé, J. & Clark, T. L. 1978 The evolution of finite amplitude Kelvin–Helmholtz billows. *Geophys. Astrophys. Fluid Dyn.* **10**, 53.

Pierrehumbert, R. T. & Widnall, S. E. 1982 The two- and three-dimensional instabilities of a spatially periodic shear layer. *J. Fluid Mech.* **114**, 59.

Ruelle, D. & Takens, F. 1971 On the nature of turbulence. *Commun. Math. Phys.* **20**, 167 (and Addendum **23**, 343).

Scorer, R. S. 1969 Mechanisms of clear air turbulence. In *Clear Air Turbulence and its Detection* (ed. Y. H. Pao & A. Goldburg). Plenum.

Smith, B. T., Boyle, J. M., Dongarron, J. J., Garbow, B. S., Ikebe, Y., Klema, V. C. & Moler, C. B. 1974 *Matrix Eigensystem Routines – EISPACK Guide.* Lecture Notes in Computer Science, vol. 6. Springer.

Stuart, J. T. 1967 On finite amplitude oscillations in laminar mixing layers. *J. Fluid Mech.* **29**, 417.

Thorpe, S. A. 1973 Experiments on instability and turbulence in a stratified shear flow. *J. Fluid Mech.* **61**, 731.

Woods, J. D. 1969 On Richardson's number as a criterion for laminar–turbulent–laminar transition in the ocean and atmosphere. *Radio Sci.* **4**, 1289.